

Contents

1	Searches for New Physics in $\tau^+\tau^-$ Final States	2
1.1	Signal Modelling	3
1.1.1	Additional Higgs Bosons	3
1.1.2	Vector Leptoquarks	6
1.2	Event Selection	8
1.2.1	Trigger Requirements	9
1.2.2	Offline Requirements	10
1.3	Search Optimisation	11
1.4	Background Modelling Overview	15
1.5	QCD Estimation in the $e\mu$ Channel	16
1.6	Embedding Method	17
1.7	Fake Factor Method	19
1.7.1	Determination Regions	20
1.7.2	Parametrisation	22
1.7.3	Corrections	26
1.7.4	Applying Fake Factors	28
1.8	MC Corrections	30
1.9	Uncertainty Model	31
1.10	Signal Extraction	35
1.11	Postfit Plots	38
1.12	Model Independent Results	39
1.12.1	Limits	39
1.12.2	Significance and Compatibility	44
1.12.3	2D Likelihood Scans	46
1.13	Model Dependent Limits	46

Chapter 1

Searches for New Physics in $\tau^+\tau^-$ Final States

The $\tau^+\tau^-$ final states are a powerful tool to search for new physics at collider experiments. As the heaviest lepton, τ particles are sensitive to resonant production of new neutral particles where the couplings have mass hierarchy. They are also sensitive to non-resonant effects from new physics mediators. This chapter will detail the searches for two such areas of new physics: additional Higgs bosons and vector leptoquarks. These searches are split up into three sections:

- i) A model independent search for single narrow spin-0 resonance (ϕ), produced via gluon fusion ($gg\phi$) or in association with a b quark ($bb\phi$). The SM Higgs boson is treated as a background and the Yukawa couplings of the spin-0 resonance that contribute to the gluon fusion loop are set to SM values.
- ii) A search for the MSSM Higgs sector in a number of benchmark scenarios. The benchmark scenarios were proposed in Refs. [1, 2, 3] and summarised in Ref. [4]. The M_h^{125} and $M_{h,\text{EFT}}^{125}$ scenarios are shown in this chapter. The production of the observed Higgs boson particle at 125 GeV is also used to constrain the available phase space.
- iii) A search for the t-channel exchange of a U_1 vector leptoquark. Two scenarios are taken, motivated by the best fit to the b anomalies. These scenarios are detailed in Section 1.1.2.

These searches are performed with the full run-2 dataset (138 fb^{-1}) collected by the CMS experiment. The search for additional Higgs bosons had previously been

performed with data collected in 2016 (39 fb^{-1}) and results were consistent with the SM background prediction [5].

1.1 Signal Modelling

1.1.1 Additional Higgs Bosons

Extended Higgs sectors, such as that of the MSSM, can be probed by direct searches for the additional bosons and further precise measurements of the SM Higgs boson. This search for an extended Higgs sector is motivated by Type II 2HDMs, such as the MSSM. In these models $\tan\beta$ enhances couplings of additional Higgs bosons to down-type quarks and leptons, whilst up-type quark couplings are suppressed. This divides the dominant production modes of the Higgs boson into two categories: Gluon fusion and production in association with a bottom quark. Examples of the Feynman diagrams for such processes are shown in Figure 1.1.

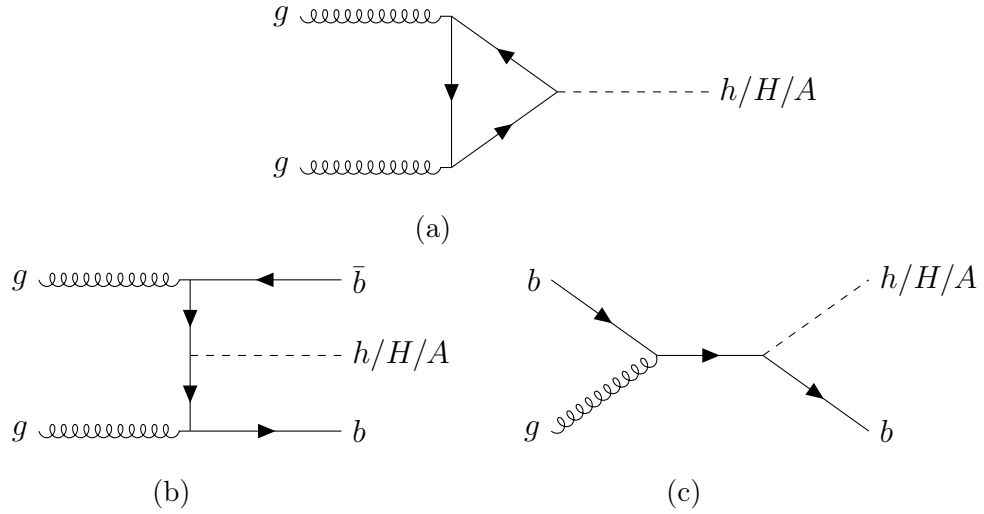


Figure 1.1: Diagram (a) shows the production of neutral Higgs bosons from gluon fusion. The dominant loop contributions to this diagrams are from top-only, bottom-only and top-bottom interference. Diagrams (b) and (c) show production in association with b quarks.

With the $\tan\beta$ enhancement, the decays of additional Higgs bosons to τ leptons and b quarks are most likely. τ leptons are identified with a higher purity than bottom quarks at the CMS detector. It is also easier to separate $\tau^+\tau^-$ from the large QCD

multijet background produced from the high energy proton-proton collisions. This hypothesis was tested with the 2016 dataset and although no deviations were observed, the strongest limits on the MSSM phase space was placed by the $\tau^+\tau^-$ final states [5, 6].

For this analysis, signal templates for the production of additional Higgs bosons over a mass range of 60 GeV to 3.5 TeV are generated. Gluon fusion is simulated at NLO precision using the 2HDM implementation of POWHEG 2.0 [7, 8, 9, 10]. The kinematic properties are highly dependent on the contributions to the loop, that are dependent on the specific signal model. To account for the different loop contributions at the NLO plus parton shower prediction, weights based off the p_T spectra are calculated to split the contributions from the t quark only, b quark only, and tb-interference. Once individual templates have been determined for each contribution to the loop, the 2HDM samples can be scaled to the MSSM scenario prediction with the following formula,

$$\begin{aligned} \frac{d\sigma_{\text{MSSM}}}{dp_T} = & \left(\frac{Y_{t,\text{MSSM}}}{Y_{t,2\text{HDM}}} \right)^2 \frac{d\sigma_{2\text{HDM}}^t(Q_t)}{dp_T} + \left(\frac{Y_{b,\text{MSSM}}}{Y_{b,2\text{HDM}}} \right)^2 \frac{d\sigma_{2\text{HDM}}^b(Q_b)}{dp_T} \\ & + \left(\frac{Y_{t,\text{MSSM}} Y_{b,\text{MSSM}}}{Y_{t,2\text{HDM}} Y_{b,2\text{HDM}}} \right) \left\{ \frac{d\sigma_{2\text{HDM}}^{t+b}(Q_{tb})}{dp_T} - \frac{d\sigma_{2\text{HDM}}^t(Q_{tb})}{dp_T} - \frac{d\sigma_{2\text{HDM}}^b(Q_{tb})}{dp_T} \right\}, \quad (1.1) \end{aligned}$$

where Q_i are resummation scales that depend on the mass of the additional Higgs boson. Further contributions from any Supersymmetric partners were checked and account for less than a few percent and so are neglected. The p_T reweighting is done separately for the scalar and pseudoscalar additional Higgs bosons, as the p_T distributions can differ. The benchmark scenarios provide the relative Yukawa couplings (to calculate the cross sections) and branching fractions of the MSSM Higgs bosons. An example of the distributions for gluon fusion production, in the MSSM M_h^{125} scenario with $m_A = 1600$ GeV and $\tan\beta$ varying, is shown in Figure 1.2. The distributions peak at a higher p_T for the top quark loop, therefore at smaller $\tan\beta$, where the top quark contribution is dominant, an additional Higgs boson would be more boosted.

Production in association with bottom quarks is simulated at NLO precision using the corresponding POWHEG 2.0 implementation in the four-flavour scheme [7, 8, 9, 10]. All additional Higgs boson signal generation is performed using the parton

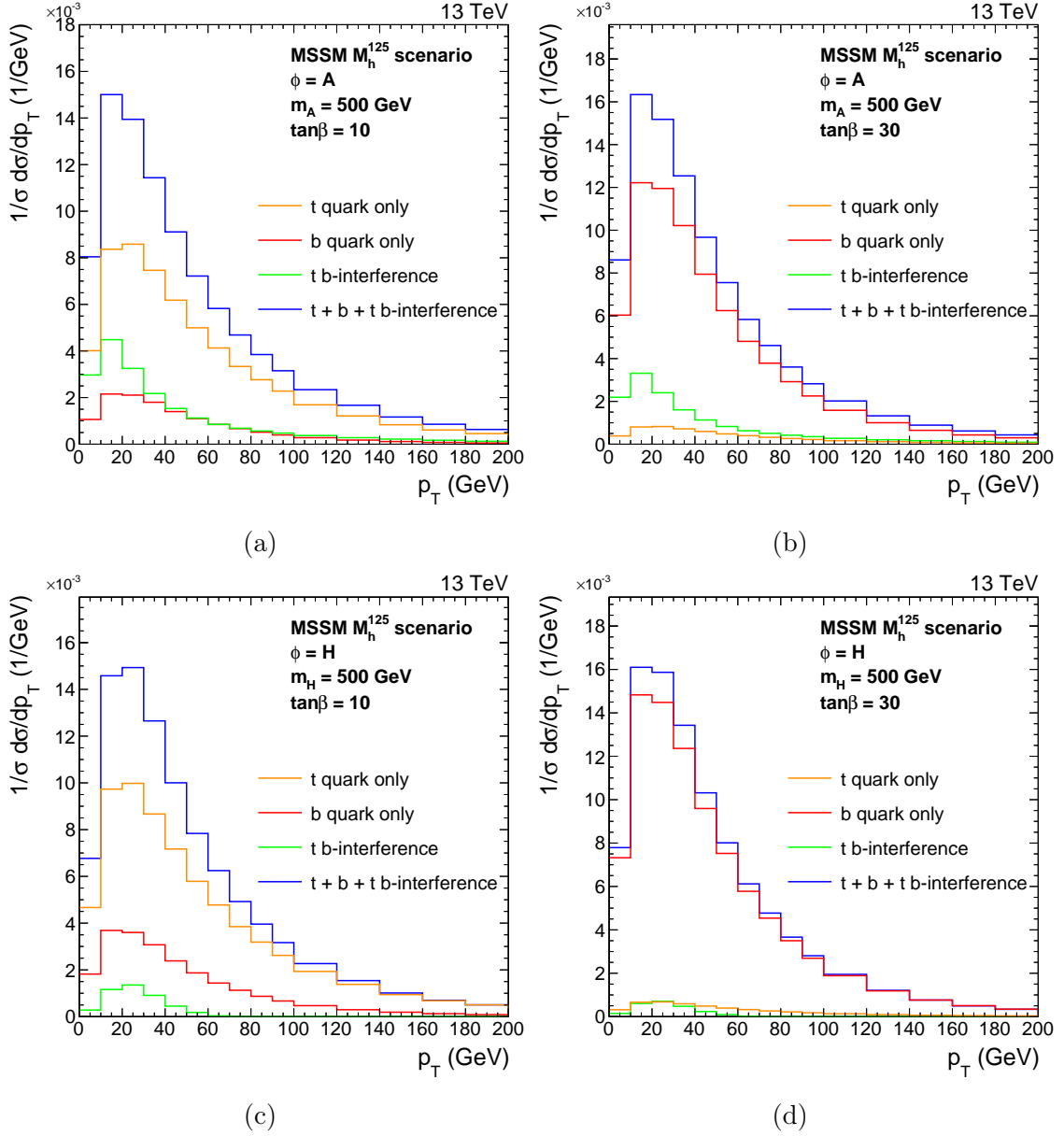


Figure 1.2: p_T density distributions of the A (top) and H (bottom) boson, with contributions to the gluon fusion loop displayed individually and summed. These are shown for $\tan\beta$ values of 10 (left) and 30 (right) where $m_A = 500$ GeV in the MSSM M_h^{125} scenario.

distribution function (PDF) NNPDF3.1 [11, 12]. τ lepton decay, parton showering and hadronisation are all modelled with the PYTHIA event generator where the PU profile is matched to data [13, 14]. All events generated are passed through a GEANT4-based [15] simulation of the CMS detector and reconstructed in the same way as data.

The model-dependent search for the MSSM also looks to find differences from the observed SM Higgs boson and the predicted MSSM SM-like Higgs boson. In each MSSM benchmark scenario, an uncertainty of ± 3 GeV is given on the prediction for the SM Higgs boson mass. This uncertainty is to reflect the contribution from any unknown higher-order corrections. The value of the mass is allowed to vary within this window, however the Yukawa couplings are rescaled the observed mass.

1.1.2 Vector Leptoquarks

The best fit to the b anomalies in the available phase space for vector leptoquarks yielded large b quark and τ lepton couplings to the U_1 particle. The possible production modes of a $\tau^+\tau^-$ final state are shown in Figure 1.3.

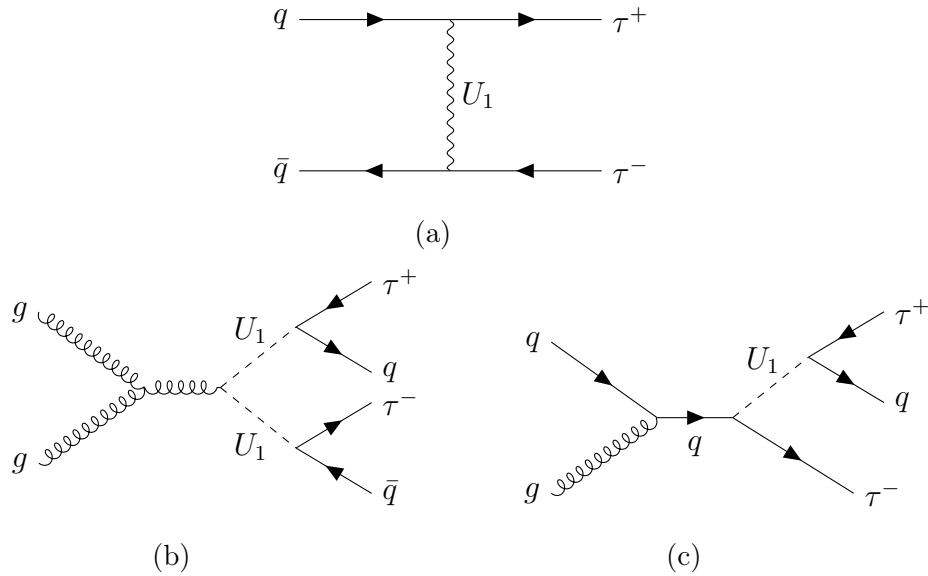


Figure 1.3: Feynman diagrams showing the contribution from U_1 vector leptoquarks to the final state with a pair of oppositely charged τ leptons. Diagram (a) shows t-channel, (b) pair and (c) single production of a vector leptoquark.

Pair and single production of a vector leptoquark are dependent on its strong coupling, which is highly model dependent. For large mass, m_U , the probability of producing an on-shell U_1 singlet or pair is heavily suppressed due to the momentum of the initial partons. These production processes are not discussed further in this search. Further studies have been used to search for single and pair production at the CMS experiment and no statistically significance derivation was observed [16]. Single production places the loosest constraints out of the processes mentioned whilst pair production puts a lower limit on the leptoquark mass, as the process is approximately independent on g_U , and this limit is heavily dependent on the values taken for the strong coupling.

The t-channel process contain two vertices with a U_1 vector leptoquark, a quark and a τ lepton, and hence the cross section will scale with g_U^4 . From the best fit to b anomalies, the vertex is dominated by the b quark and hence the initial state will be mostly from $b\bar{b}$, with sub-dominant contributions from $b\bar{s}$, $s\bar{b}$ and $s\bar{s}$. Although there are no additional b quarks in the final state in the LO process, initial state radiation can lead to additional b quarks in the final state. In this search the two scenarios discussed in Section ?? are considered. The only non negligible freely floating parameter in each fit, for $\tau^+\tau^-$ final states in the m_U - g_U phase space is the $\beta_L^{s\tau}$ parameter. This is set to the best fit value.

The signal process of the U_1 t-channel exchange is simulated in the five-flavour scheme (5FS) at LO precision using the MADGRAPH5_aMC@NLO v2.6.5 event generator [17]. Events are generated with one or fewer outgoing partons from the matrix element and the MLM prescription [18] is then used for matching, with a scale set to 40 GeV. Negligible dependence of the U_1 decay width is observed, for simulation this is chosen to approximately match the value predicted by the b anomaly fit. Samples with a mass between 1 and 5 TeV at $g_U = 1$ are generated.

The interference between the U_1 signal and $Z/\gamma^* \rightarrow \tau\tau$ production was checked and a large destructive affect was observed, with magnitude dependent on g_U . To account for this, separate samples are produced for this interference, generated in the same way as the t-channel exchange. The interference samples are then split into two with a di- τ mass split in order to have a sufficient number of events in the high di- τ mass regions. The cross section of these interference samples scale with g_U^2 . Examples of the generator level di- τ mass distributions are shown in Figure 1.4.

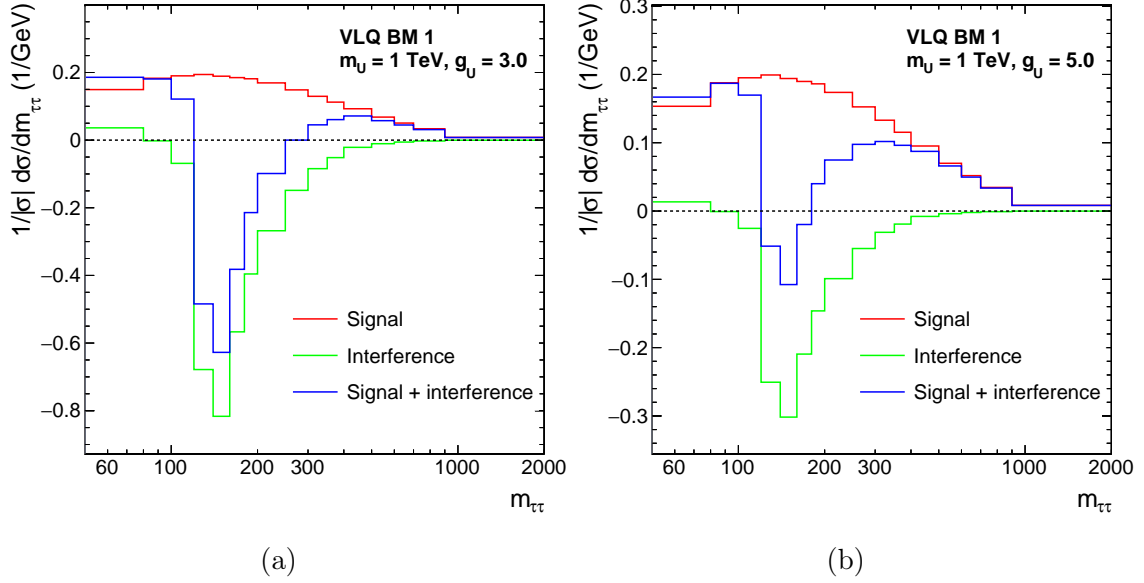


Figure 1.4: The generator level $m_{\tau\tau}$ density distributions of the t-channel vector leptoquark signal and the interference with Drell-Yan. This is shown in the VLQ BM 1 scenario for a leptoquark of mass 1 TeV for coupling strengths of $g_U = 3$ (a) and $g_U = 5$ (b).

The t-channel signal produces a broad distribution in $m_{\tau\tau}$ due to its non-resonant nature. The interference is mostly a destructive effect (except for at small $m_{\tau\tau}$), with the yield becoming less negative at higher $m_{\tau\tau}$. The interference peaks negatively between 100 and 200 GeV and in this region the combined yield can be negative. Due to the difference in scaling of the two effects, at small g_U the interference is more dominant than the signal and hence the yield of the combined result is reduced.

1.2 Event Selection

The possible decays of two τ leptons and their branching fractions, where the τ decay is grouped into three categories e , μ and τ_h as defined in Section ??, are shown in Table 1.1. For this search the four largest branching fraction channels used: $\tau_h\tau_h$, $e\tau_h$, $\mu\tau_h$ and $e\mu$. This accounts for approximately 94% of di- τ events. The two same lepton channels are neglected due to small branching ratio and the dominating $Z \rightarrow ee$ and $Z \rightarrow \mu\mu$ backgrounds.

Channel	Branching Fraction
$\tau_h\tau_h$	42.0%
$e\tau_h$	23.1%
$\mu\tau_h$	22.6%
$e\mu$	6.2%
ee	3.2%
$\mu\mu$	3.0%

Table 1.1: Branching fractions of the decays of two τ leptons.

1.2.1 Trigger Requirements

In the four final state pairs, a number of different online trigger requirements are needed. In the $\tau_h\tau_h$ channel, two possible triggers are available: the double- τ_h and single- τ_h triggers. The single- τ_h trigger has a high p_T threshold at 120 (180) GeV for events recorded in 2016 (2017-2018), whilst the double- τ_h has a p_T threshold at 40 GeV. Therefore, the double- τ_h trigger is used individually where the τ_h has p_T below the single- τ_h threshold and the union of single- τ_h and double- τ_h triggered events are taken above the threshold.

In the $e\tau_h$ and $\mu\tau_h$ channels, there are three possible triggers available: the single- e/μ , single- τ_h and the e/μ - τ_h cross-trigger. The cross-trigger is used for events where the light lepton has p_T between the thresholds for the cross-trigger and single- e/μ shown in Table 1.2. The light lepton used in the cross-trigger is required to be in the central barrel of the detector within $|\eta| < 2.1$. Above these light lepton p_T thresholds the single- e/μ trigger is used, where it is required that the τ_h has $p_T > 30$ GeV. At τ_h p_T above the single- τ_h thresholds, the single- τ_h trigger is used in combination with the single- e/μ trigger.

Year/ Trigger	$e\tau_h$ cross-trigger	single- e	$\mu\tau_h$ cross-trigger	single- μ
2016	23	26	20	23
2017	25	28	20	25
2018	25	33	21	25

Table 1.2: Lower trigger light lepton thresholds p_T in GeV for the $e\tau_h$ and $\mu\tau_h$ channels.

In the $e\mu$ channel, there are three possible triggers available: the single- e , single- μ and the $e\mu$ cross-trigger. However, only the cross-trigger is used in this analysis, due to the larger efficiencies of correctly selecting light leptons. The e and μ are required to have $p_T > 15$ GeV and $|\eta| < 2.4$.

1.2.2 Offline Requirements

All offline selections stated are in addition the object selection discussed in Section ???. In this analysis, τ_h candidates are required to pass the **Medium** $D_{\text{jet}}^{\text{WP}}$. D_e^{WP} and D_μ^{WP} are dependent on the decay channel. The **VVLoose**, **Tight**, **VVLoose** D_e^{WP} and the **VLoose**, **VLoose** and **Tight** D_μ^{WP} are used in the $\tau_h\tau_h$, $e\tau_h$ and $\mu\tau_h$ channels respectively. The tighter working point for the same light lepton discrimination as tagged in the event is used to remove light leptons misidentified as τ_h from the $Z \rightarrow ll$ process. The light lepton isolation requirement is $I_{\text{rel}}^{e/\mu} < 0.15$ except for in the $e\mu$ channel where the muon is required to have $I_{\text{rel}}^\mu < 0.2$.

The selected τ lepton decay candidates are required to have opposite charge and to be separated by more than $\Delta R > 0.5$ in all channels except $e\mu$ where $\Delta R > 0.3$. In events where the numbers of an object in the event is greater than the required number of objects in the $\tau\tau$ decay channel, the objects are sorted by the maximum $D_{\text{jet}}^{\text{score}}$ if a τ_h candidate or minimum I_{rel} if a light lepton candidate and the leading objects are chosen. In order to maintain orthogonality between channels, events with additional light leptons passing looser selections than the nominal requirements, are rejected from the selection. The looser selections help to suppress the $Z \rightarrow ll$ background process further.

In the $e\tau_h$ and $\mu\tau_h$ channels, a cut is placed at 70 GeV on the transverse mass between the light lepton \vec{p}_T and the missing \vec{p}_T , where the transverse momentum is defined as,

$$m_T(\vec{p}_T^i, \vec{p}_T^j) = \sqrt{2p_T^i p_T^j (1 - \cos \Delta\phi)}, \quad (1.2)$$

where $\Delta\phi$ to the azimuthal angle between \vec{p}_T^i and \vec{p}_T^j . The variable is used to remove $W + \text{jets}$ background events, where a jet is misidentified as a τ_h and the MET and light lepton from the W decay are aligned and hence the event has a large $m_T(\vec{p}_T^{e/\mu}, \vec{p}_T^{\text{MET}})$.

In the $e\mu$ channel, an additional cut is placed on the variable D_ζ , which is defined

as,

$$D_\zeta = p_\zeta^{\text{miss}} - 0.85p_\zeta^{\text{vis}}; \quad p_\zeta^{\text{miss}} = \vec{p}_T^{\text{miss}} \cdot \hat{\zeta}; \quad p_\zeta^{\text{vis}} = (\vec{p}_T^e + \vec{p}_T^\mu) \cdot \hat{\zeta} \quad (1.3)$$

where $\vec{p}_T^{e/\mu}$ corresponds to the transverse momentum vector of the electron or muon and $\hat{\zeta}$ to the bisectonal direction between the electron and the muon in the transverse plane. A diagram of the inputs is shown Figure 1.5.

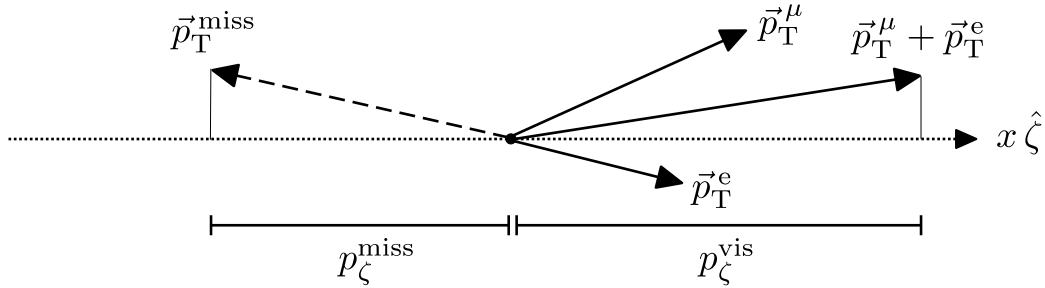


Figure 1.5: Diagram of inputs to the D_ζ variable.

The linear combination is optimised for genuine di- τ events to peak around $D_\zeta = 0$ GeV. It is motivated by the expectation that in di- τ decays from a resonance, the visible and missing (from τ neutrinos) momenta are roughly aligned and of similar magnitudes. In $W + \text{jets}$ and $t\bar{t}$ events the directions of the visible and missing products are expected to be more randomly distributed and lead to a non-peaking D_ζ . Therefore, only events with $D_\zeta > -35$ GeV are considered for signal events. Events with no b tag with this cut are vetoed and events with a b tag also with this cut are used for a $t\bar{t}$ control region and discussed further in Section 1.4.

1.3 Search Optimisation

The optimisation of the signal extraction depends on which of the three scenarios, set out at beginning of this section, is searched for. The components of the optimisation are named the high-mass, low-mass and SM Higgs optimisation procedures. For the model independent search (i) the high- or low-mass optimisation procedures are used depending on whether the mass of the resonance is greater or less than 250 GeV. The search for the MSSM Higgs sector (ii) uses the high mass or the SM Higgs optimisation procedures depending on whether the reconstructed di- τ mass is greater or less than 250 GeV. Due to more than one neutrino in the event, it is

not possible to fully reconstruct the di- τ mass. To resolve this issue a likelihood-based method named SVFit algorithm is used [19]. Finally, the search for vector leptoquarks (iii) uses only the high mass optimisation procedure. The procedures are discussed in detail below.

The high-mass optimisation procedure follows what was done in Ref. [5]. Each event is initially split into categories depending on whether it has 0 or ≥ 1 b tagged jets in the event. Firstly, this helps target the additional Higgs boson production modes gluon fusion and b associated production respectively. In particular, $bb\phi$ has final state b quarks that if tagged can significantly aid the sensitivity of this signal. Secondly, the initial state radiation of a t-channel vector leptoquark signal dominated by initial states of b quarks, can lead to additional b jets in the final state. The reduced backgrounds in b tagged events allows for a more sensitive vector leptoquark search in this category.

The $e\tau_h$ and $\mu\tau_h$ channels are further subdivided into categories depending on the transverse mass between the light lepton and missing transverse momentum vectors as defined in Equation 1.2. The corresponding categories are defined as:

- **Tight- m_T** : $m_T(\vec{p}_T^{e/\mu}, \vec{p}_T^{\text{miss}}) < 40$ GeV;
- **Loose- m_T** : $40 \leq m_T(\vec{p}_T^{e/\mu}, \vec{p}_T^{\text{miss}}) < 70$ GeV.

The majority of the signal events fall within the **Tight- m_T** sub-category. The **Loose- m_T** category is used to improve the signal acceptance for resonant masses of $m_\phi > 700$ GeV.

In the $e\mu$ channel, is subdivided into three signal categories based on the cuts on the variable D_ζ as defined in Equation 1.3. The three categories are defined as:

- **Low- D_ζ** : $-35 \leq D_\zeta < -10$ GeV;
- **Medium- D_ζ** : $-10 \leq D_\zeta [\text{GeV}] < 30$ GeV;
- **High- D_ζ** : $D_\zeta [\text{GeV}] \geq 30$ GeV.

By design, the majority of signal events are located in the **Medium- D_ζ** sub-category. The **Low-** and **High- D_ζ** categories are used to catch the tail of the signal distributions. A schematic of all high mass optimisation categories are shown in Figure 1.6.

Once all category divisions have been applied, events are drawn in histograms based off a discriminating variable. The discriminating variable used in this analysis is m_T^{tot} and is defined below.

$$m_T^{\text{tot}} = \sqrt{m_T(\vec{p}_T^{\tau_1}, \vec{p}_T^{\text{miss}})^2 + m_T(\vec{p}_T^{\tau_2}, \vec{p}_T^{\text{miss}})^2 + m_T(\vec{p}_T^{\tau_1}, \vec{p}_T^{\tau_2})^2}, \quad (1.4)$$

where τ_1 and τ_2 refer to the visible products of the two τ lepton decays. This variable provides excellent discriminating power between higher mass resonant signals compared to other non-peaking backgrounds, whilst still maintaining some separation between signal masses. It is also excellent at separating the high-mass non-resonant di- τ signatures where a di- τ mass is unphysical for the signal. This is due to the use of the transverse momenta and MET in the variable definition. For a t-channel signal where the mediator has high mass, no significant mass separation is expected in any variable.

The low-mass optimisation procedure loosely follows the high-mass procedure with a few key difference. Firstly, categories that are only sensitive to high-mass signals are dropped. This includes the **Low- D_ζ** and **Loose- m_T** categories. Each no b tag subcategory is further divided into four bins of reconstructed di- τ visible p_T with bin edges: 0,50,100,200 and ∞ . This is not done in the b tag subcategories due to the lack of statistics in this region. A schematic of the categories used in the low mass optimisation procedure is shown in Figure 1.7. The final difference with the high-mass optimisation procedure is the discriminator used. In the low-mass optimisation procedure the reconstructed di- τ mass is used. This helps to separate signal events from the Z boson peak in this region.

Finally, the SM Higgs optimisation procedure is taken from the CMS SM $H \rightarrow \tau\tau$ analysis and is detailed in Ref. [20]. This was previously used for simplified template cross section measurements. This uses a neural-network-based (NN) categorisation to obtain the most precise estimates from data of the SM Higgs produced via gluon fusion, vector boson fusion or vector boson associated production. The NN based analysis introduces 26 categories, 8 of which are optimised to pull out the Higgs boson signal. Although the NN is trained specifically to target events with an SM-like Higgs boson, signal events with differing masses can also enter the NN categories.

	No b tag			b tag		
$e\mu$	Low- D_ζ	Medium- D_ζ	High- D_ζ	Low- D_ζ	Medium- D_ζ	High- D_ζ
$e\tau_h$	Loose- m_T		Tight- m_T	Loose- m_T		Tight- m_T
$\mu\tau_h$	Loose- m_T		Tight- m_T	Loose- m_T		Tight- m_T
$\tau_h\tau_h$						
$t\bar{t}(e\mu)$				<div>$D_\zeta < -35 \text{ GeV}$</div>		
	<div><div></div>Signal region (SR)</div>					
	<div><div></div>Control region</div>					

Figure 1.6: Overview of the categories used for the extraction of the signal in the high mass optimisation procedure.

		No b tag		b tag	
$e\mu$	Medium- D_ζ	High- D_ζ	Medium- D_ζ	High- D_ζ	
	$p_T^{\tau\tau} < 50 \text{ GeV}$	$p_T^{\tau\tau} < 50 \text{ GeV}$			
	$50 < p_T^{\tau\tau} < 100 \text{ GeV}$	$50 < p_T^{\tau\tau} < 100 \text{ GeV}$			
	$100 < p_T^{\tau\tau} < 200 \text{ GeV}$	$100 < p_T^{\tau\tau} < 200 \text{ GeV}$			
	$p_T^{\tau\tau} > 200 \text{ GeV}$	$p_T^{\tau\tau} > 200 \text{ GeV}$			
$e\tau_h$	Tight- m_T		Tight- m_T		
	$p_T^{\tau\tau} < 50 \text{ GeV}$				
	$50 < p_T^{\tau\tau} < 100 \text{ GeV}$				
	$100 < p_T^{\tau\tau} < 200 \text{ GeV}$				
	$p_T^{\tau\tau} > 200 \text{ GeV}$				
$\mu\tau_h$	Tight- m_T		Tight- m_T		
	$p_T^{\tau\tau} < 50 \text{ GeV}$				
	$50 < p_T^{\tau\tau} < 100 \text{ GeV}$				
	$100 < p_T^{\tau\tau} < 200 \text{ GeV}$				
	$p_T^{\tau\tau} > 200 \text{ GeV}$				
$\tau_h\tau_h$					
	$p_T^{\tau\tau} < 50 \text{ GeV}$				
	$50 < p_T^{\tau\tau} < 100 \text{ GeV}$				
	$100 < p_T^{\tau\tau} < 200 \text{ GeV}$				
	$p_T^{\tau\tau} > 200 \text{ GeV}$				
$t\bar{t}(e\mu)$			$D_\zeta < -35 \text{ GeV}$		
		Signal region (SR)			
		Control region			

Figure 1.7: Overview of the categories used for the extraction of the signal in the low mass optimisation procedure.

1.4 Background Modelling Overview

The analysis considers several backgrounds including Drell-Yan, $t\bar{t}$, W+jets, QCD, di-boson, single-top, and electroweak W and Z bosons production. These are split into a five categories:

- i) Events containing only genuine τ leptons.
- ii) Events with a jet misidentified as a τ_h (jet $\rightarrow \tau_h$) in the $e\tau_h$, $\mu\tau_h$ or $\tau_h\tau_h$ channels.
- iii) Events with jets faking both light leptons (jet $\rightarrow l$) in the $e\mu$ channel.
- iv) Events from $t\bar{t}$ with a prompt light lepton (e or μ not from a τ decay) and the other object (if there are not two prompt light lepton) is from a genuine τ leptons.
- v) Other events. This is a small contribution and hence why it is grouped.
 - Non $t\bar{t}$ events with a prompt light lepton (e or μ not from a τ decay) and the other object (if there are not two prompt light lepton) is from a genuine τ leptons.
 - Events with a light lepton misidentified as a τ_h and the other object (if there are not two light leptons faking a τ_h) is reconstructed as prompt light lepton or from genuine τ leptons.
 - Events with a jet misidentified as a light lepton and the other object is from genuine τ leptons in the $e\tau_h$, $\mu\tau_h$ or $\tau_h\tau_h$ channels.
 - Events with a muon misidentified as an electron in the $e\mu$ channel.
 - Events with one jet misidentified as a light lepton and the other object from a prompt light lepton in the $e\mu$ channel.

Backgrounds from (i) consists of largely $Z/\gamma^* \rightarrow \tau\tau$ events but there are also smaller contributions from other processes. This background is modelled by a data-simulation hybrid method called the embedding method and this is described in detail in Section 1.6. Group (ii) is dominated by QCD, W + jets and $t\bar{t}$ events with a jet $\rightarrow \tau_h$ misidentification. This is modelled from data by the fake factor method (F_F) and is explained in Section 1.7. Group (iii) is modelled from data to describe the QCD multijet contribution to the background in the $e\mu$ channel. The method to obtain this background is described in Section 1.5. The data driven

background estimations for (i), (ii) and (iii) contribute $\approx 98\%$ of all expected background events in the $\tau_h\tau_h$ channel, $\approx 90\%$ in $e\tau_h$ and $\mu\tau_h$ channels and $\approx 50\%$ in the $e\mu$ channel. The final groups, (iv) and (v), are modelled with MC. The $t\bar{t}$ process is separated due to its large contribution to the phase space where a b jet is required.

In 2016 (2017–2018), the $W + \text{jets}$ and $Z \rightarrow ll$ processes are simulated using the MADGRAPH5_aMC@NLO 2.2.2 (2.4.2) event generator at leading order (LO) [17]. Supplementary samples are generated with up to four outgoing partons in the hard interaction to increase the number of simulated events in regions of high signal purity. For diboson production, MADGRAPH5_aMC@NLO is used at next-to-LO (NLO) precision [17], and the FxFx [18] (MLM [21]) prescription is used to match the NLO (LO) matrix element calculation with the parton shower model. Samples for $t\bar{t}$ [22] and (t-channel) single top quark production [23] are generated at NLO precision using POWHEG 2.0 [7, 8, 9, 10], and for single top quark production in association with a W boson (tW channel) [24], POWHEG version 1.0 at NLO precision is used. When compared with data, $W + \text{jets}$, $Z \rightarrow ll$, $t\bar{t}$, and single top quark events in the tW channel are normalised to their cross sections at next-to-next-to-LO (NNLO) precision [25, 26, 27], while single top quark (t-channel) and diboson events are normalized to their cross sections at NLO precision or higher [27, 28, 29].

1.5 QCD Estimation in the $e\mu$ Channel

The QCD model in the $e\mu$ channel, that attempts to model events where two jets are misidentified as an electron muon pair, is taken from data with a same-sign pair with a transfer factor (F_T). The transfer factor determines differences from the same-sign to opposite-sign region and is calculated from a sideband region with an anti-isolated muon ($0.2 < I_{\text{rel}}^\mu < 0.5$). F_T is initially parameterised by the ΔR between the electron and muon, and the number of jets in the event, however additional dependencies on the electron and muon p_T enter via a correction.

Good agreement is observed in events with no b jets, when applying F_T onto same sign events compared to opposite sign events where both regions have an anti-isolated muon. However, in events with b jets an additional correction is needed. This is determined to be ≈ 0.75 (differs very slightly between data taking years). As this correction is large, it is validated by switching the light lepton anti-isolation, so that the electron is required to have $0.15 < I_{\text{rel}}^e < 0.5$. Also, events where both light leptons are anti-isolated are looked at. The correction for b tagged events is equivalent

in all three regions, and a global average of the three is taken for the final correction.

To understand the physical reason for the large difference in no b tag and b tag events in same sign and opposite pairs, studies were performed on simulated samples. It was observed that the electron-muon pair is usually produced from pairs of heavy quarks, $pp \rightarrow b\bar{b} (c\bar{c})$. If the two jets are initiated from the heavy quarks there is a large bias towards opposite sign jets due to the opposite signs of the quark anti-quark pair. However, if one of the heavy quarks is tagged as a b jet, another object has to be the jet initiator (a radiated gluon for example) and there is therefore no charge preference in the pair. As F_T is originally fit inclusively in numbers of b jets and the 0 bin is dominant, the correction over predicts the opposite sign to same sign ratio and so a large correction is needed as observed.

1.6 Embedding Method

The background for genuine di- τ lepton pairs is modelled via the embedding method. This is a hybrid method that utilises both data and MC techniques to produce high statistic samples, where the bulk of the event comes from data. This minimises both the chance of MC fluctuations and the size of the uncertainties. The background is dominated by $Z \rightarrow \tau\tau$ decay however there will be smaller contributions from $t\bar{t}$ and di-boson processes.

The algorithm first selects $\mu\mu$ events from data. The selection is chosen to naturally target the pure $Z \rightarrow \mu\mu$ region but still be loose enough to catch events from other processes, so not to introduce a bias on the Z boson mass. Events are required to pass the double- μ trigger with minimum requirements on the invariant mass of the two muons ($m_{\mu\mu}$) and the p_T of the leading and trailing muon. Also required at the trigger level is a loose association of the track to the PV and a loose isolation in the tracker. Offline objects matched to the trigger muons, are then required to have standard d_z and η selections and originate from a global muon-track, as defined in Section ???. The muon pair are required to have opposite charge and have $m_{\mu\mu} > 20$ GeV. The fraction of processes within this selection is tested with MC background samples and a QCD model from same sign muon pairs with an extrapolation factor. Approximately 97% of selected events are expected to come from $Z \rightarrow \mu\mu$ events with smaller contributions from $Z \rightarrow \tau\tau$ ($\tau \rightarrow \mu$), di-boson, $t\bar{t}$ and QCD. The di-boson and $t\bar{t}$ relative contributions are greater at higher $m_{\mu\mu}$ and in

events with tagged b jets whilst the QCD contribution is largest at lower $m_{\mu\mu}$. The events selected are biased by detector acceptances. Therefore, corrections on the reconstruction and identification efficiencies are performed in muon η and p_T using the "tag-and-probe" method.

Next, all energy deposits in the detector from the selected muons are removed. This involves removing the hits on global-muon track in the tracker, hits in the muons systems and clusters in the calorimeters that intercept the muon trajectory. Once completed, the selected muons and their kinematic properties are replaced with a τ lepton. To account for the difference in mass between the muon and τ , the muons are boosted into the center-of-mass frame of the di-muon system and then this 4-vector is taken for the τ but boosted back into the laboratory frame. The event simulation is performed from the PV. The τ lepton decay is then simulated with PYTHIA [13, 14] and separate samples are produced for different $\tau\tau$ decay channels. Only the decay of the τ leptons are then processed through the detector simulation and the remainder of the $\mu\mu$ event is added back. A schematic of the process is shown in Figure 1.8.

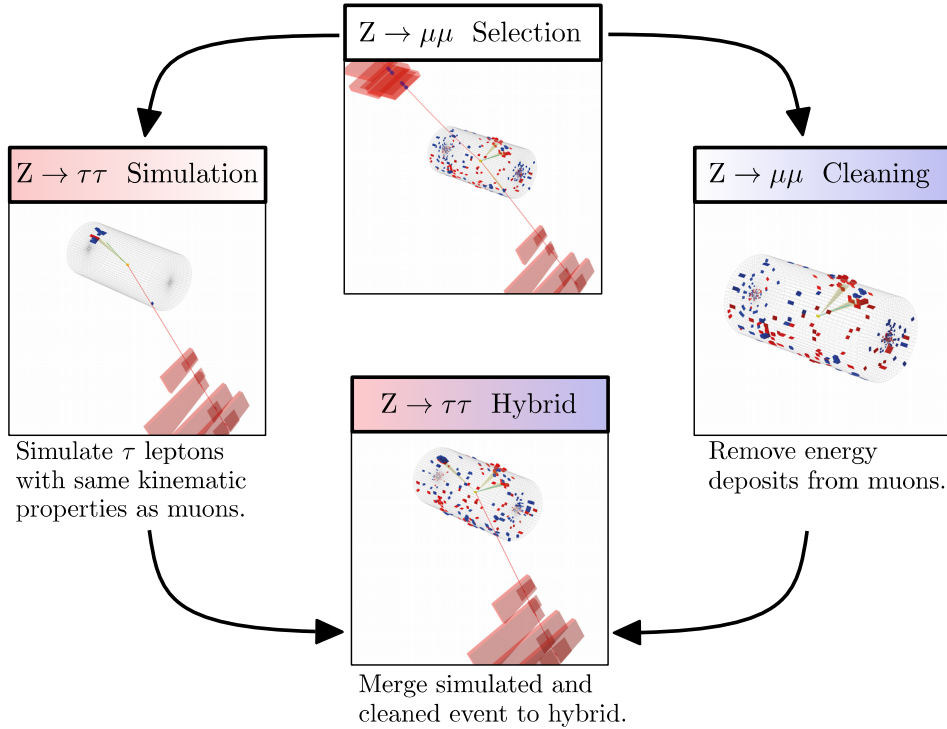


Figure 1.8: Schematic of the embedding method to model genuine di- τ backgrounds from di-muon events in data.

The embedding method is validated on dedicated samples, where the muons from data are replaced by simulated muons instead of τ leptons. A plot of the agreement from these dedicated samples with data is shown in Figure 1.9.

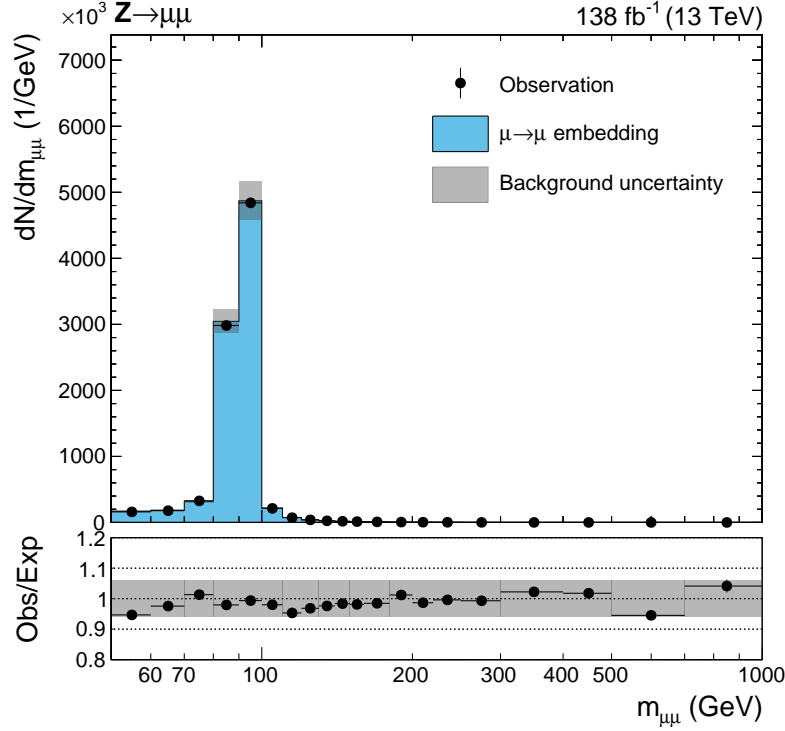


Figure 1.9: Closure plot showing the di-muon mass on the dedicated embedding validation samples.

1.7 Fake Factor Method

Backgrounds in which a jet is misidentified as a τ_h can be difficult to model using MC due to the poor description of the $\text{jet} \rightarrow \tau_h$ fake rate in simulation. In addition, the small probability of a jet being misidentified as a τ_h necessitates the production of high statistics MC samples at a significant computational expense. These shortcomings motivate the use of data-driven estimates for these processes. One such procedure is the fake factor (F_F) method.

The F_F method utilises regions in the data to model the $\text{jet} \rightarrow \tau_h$ background. Firstly, the determination regions, which are $\text{jet} \rightarrow \tau_h$ enriched control regions orthogonal to the signal region. It is used to calculate F_F by taking the ratio of number of $\text{jet} \rightarrow \tau_h$ events that pass the nominal τ_h ID requirement ($N(\text{Nominal})$), to the

number of jet fake events that fail the nominal τ_h ID but pass a looser alternative τ_h ID requirement ($N(\text{Alternative} \ \&\& \ !\text{Nominal})$), as shown in Equation 1.5.

$$F_F = \frac{N(\text{Nominal})}{N(\text{Alternative} \ \&\& \ !\text{Nominal})}. \quad (1.5)$$

In the remaining text this numerator and denominator are referred to as the pass and fail regions. The derivation of this ratio is done differentially with respect to key parameters that differ in the two regions. Once F_F have been derived it is common to calculate corrections in other sideband regions (a region orthogonal to the signal region) and combine F_F measured from different processes. Finally, the F_F are applied to the application region (AR). This is defined as the SR but with the criteria that the $\text{jet} \rightarrow \tau_h$ events fail the nominal τ_h ID but pass the looser alternative τ_h ID requirement. This now models the background from $\text{jet} \rightarrow \tau_h$ events in SR.

The following Sections 1.7.1–1.7.4 detail the complexities of how this method is applied to this analysis. For these searches the nominal τ_h ID used is the **Medium** $D_{\text{jet}}^{\text{WP}}$ and the alternative τ_h ID used is the **VV Loose** $D_{\text{jet}}^{\text{WP}}$.

1.7.1 Determination Regions

The fake factors are measured separately in each year of data taking period (2016, 2017, 2018), in each channel containing a τ_h ($e\tau_h$, $\mu\tau_h$, $\tau_h\tau_h$) and in enriched regions of dominant processes that contribute $\text{jet} \rightarrow \tau_h$ events. In the $e\tau_h$ and $\mu\tau_h$ channels F_F are measured for three processes: QCD, $W + \text{jets}$ and $t\bar{t}$. In the $\tau_h\tau_h$ channel F_F are measured only for the dominant QCD process. The QCD process is assumed to produce two jet fakes and so the fake factors is chosen to be calculated from leading p_T τ_h candidate only. Section 1.7.4 discusses how single jet fake events in the $\tau_h\tau_h$ channel are modelled.

Each separate measurement region is split into three sideband regions based off two cuts that surround the signal region. These regions are named the **Determination Region (A)**, **Alternative Determination Region (B)** and **Correction Region (D)** and are schematically shown in Figure 1.10.

Region A is used to measure and fit fake factors. Region B is an alternative region used to measure and fit fake factor to account for the difference in fake factors between A and C. These alternative fake factors are applied to the fail region in D

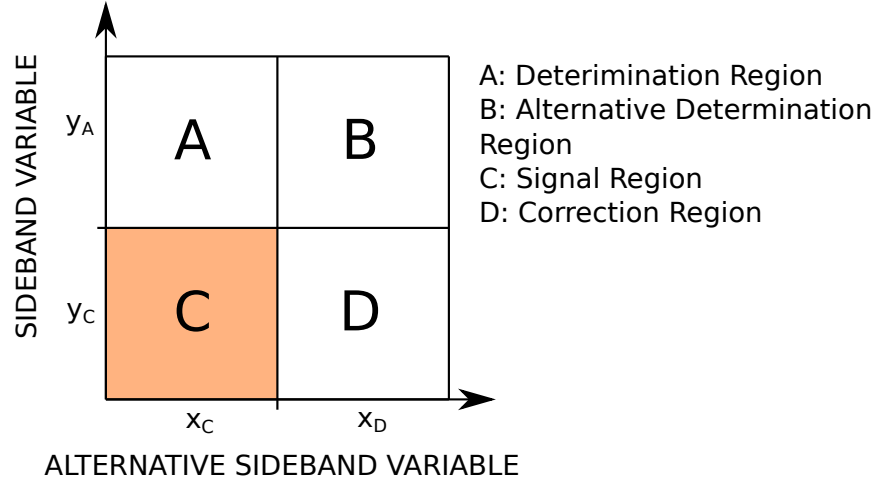


Figure 1.10: Schematic of the regions used for fake factor derivation.

and corrections are calculated comparing it to the pass region in D. The total fake factor per measurement region is calculated as the fake factors derived in region A multiplied by the correction calculated from region B to D.

The selection for x_C , x_D , y_C and y_A , as defined in Figure 1.10, in each separate measurement region are shown below. These are chosen to balance the number of events and the purity of each background in the region.

i) $\tau_h\tau_h$ QCD

y_C : The τ_h candidates are required to have the opposite sign.

y_A : The τ_h candidates are required to have the same sign.

x_C : The subleading τ_h passes the Medium $D_{\text{jet}}^{\text{WP}}$.

x_D : The subleading τ_h fails the VVLoose $D_{\text{jet}}^{\text{WP}}$ but passes the VVLoose $D_{\text{jet}}^{\text{WP}}$.

ii) $e\tau_h$ and $\mu\tau_h$ QCD

y_C : The e/μ and τ_h candidates are required to have the opposite sign.

y_A : The e/μ and τ_h candidates are required to have the same sign and the e/μ to have $I_{\text{rel}} > 0.05$.

x_C : The e/μ candidate is required to have $I_{\text{rel}} < 0.15$.

x_D : The e/μ candidate is required to have $0.25 < I_{\text{rel}} < 0.5$.

iii) $e\tau_h$ and $\mu\tau_h$ W + Jets

y_C : The m_T between the e/μ and the MET < 70 GeV.

y_A : The m_T between the e/μ and the MET > 70 GeV and no b jets in the event.

x_C : Data.

x_D : W + Jets MC.

iv) $e\tau_h$ and $\mu\tau_h t\bar{t}$

y_C : Data.

y_A : MC ($t\bar{t}$ in B and W + Jets D).

x_C : $m_T < 70$ GeV.

x_D : $m_T > 70$ GeV and no b jets.

In the $\mu\tau_h$ and $e\tau_h$ channels, W + jets $\text{jet} \rightarrow \tau_h$ events are in general the most significant and QCD contributes a smaller fraction. $t\bar{t}$ inclusively is small but becomes more significant when searching for events with a b jet. The additional $I_{\text{rel}} > 0.05$ requirement in these channels for QCD is to reduce processes producing genuine leptons and the $N_{\text{b-jets}} = 0$ requirement for W + Jets is to reduce $t\bar{t}$ contamination. It is not possible to define a DR that is sufficiently pure in $t\bar{t}$ events to make a reasonable measurement of $F_F^{t\bar{t}}$ from data. Therefore $F_F^{t\bar{t}}$ are derived from MC. A comparison of the $F_F^{W+\text{jets}}$ measured in data and MC shows only $\sim 10\text{--}20\%$ differences in the fake rates in data and MC. This observation coupled with the fact that the $t\bar{t}$ contribution is small compared to the other processes means that any bias introduced by using $F_F^{t\bar{t}}$ measured in MC is small compared to the uncertainties on the fake factors, discussed in Section 1.9.

1.7.2 Parametrisation

The raw F_F^i take into account dependencies on N_{jets} via the analysis tailed variable $N_{\text{pre b jets}}$, the p_T of the τ_h candidate ($p_T^{\tau_h}$) and the p_T of the jet matched in ΔR to the τ_h (p_T^{jet}). $N_{\text{pre b jets}}$ is defined to map the dependence of F_F^i on N_{jets} and describe the categorising variable $N_{\text{b jets}}$ well. Although not local to the τ_h , it helps control other dependencies on the constituents of the event. It is the number of jets in the event with $|\eta| < 2.4$ and $p_T > 20$. These are the same η and p_T thresholds required for a b jet. The data is split into two bins of $N_{\text{pre b jets}}$, equal to 0 and greater than 0. It is then further split by the ratio of p_T^{jet} to $p_T^{\tau_h}$. An example of the dependence of these two transverse momenta on the fake factor is shown in Figure 1.11.

It is motivated by the observation that the fake factor is largest when the p_T^{jet} and

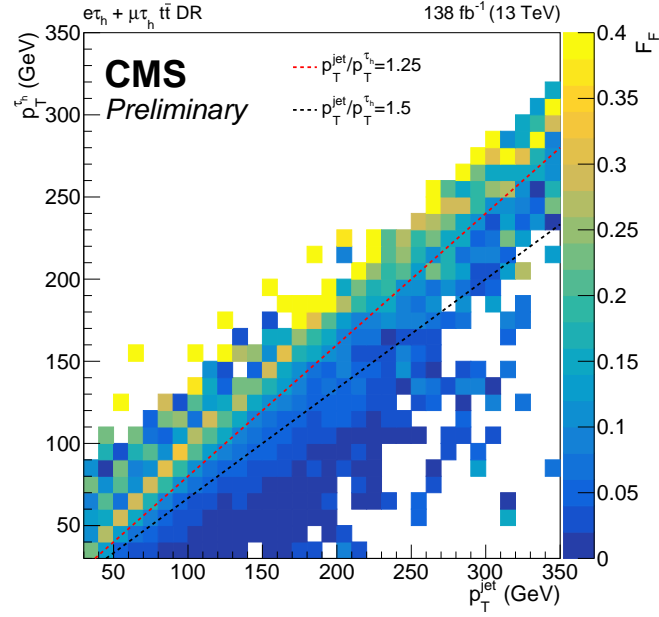


Figure 1.11: A 2D heat map of the fake factors determined from $t\bar{t}$ MC for the full run-2 dataset in the combined $e\tau_h$ and $\mu\tau_h$ channels. This is shown with respect to the τ_h p_T and the p_T of the jet matched to the τ_h . The ratio of jet to τ_h p_T categorisation used is shown split by the dashed lines.

$p_T^{\tau_h}$ are closest. The physical motivation for this is when they are close, the τ_h candidate is likely to be isolated from any other hadronic activity and so more likely to be identified as a τ . However, when p_T^{jet} is larger than $p_T^{\tau_h}$, the candidate is likely surrounded by other hadronic activity and so more likely to be a jet fake. When p_T^{jet} is less than $p_T^{\tau_h}$, charge pions are likely not close enough to the PV to be clustered into the jet and so the event is more likely to be classified as a jet fake. This will then lead to the fake factor dependence as seen in Figure 1.11.

For all divisions of the phase space, dependence on the $p_T^{\tau_h}$ is fit using the superposition of a Landau and a zeroth order polynomial in the low- p_T region. The fake factors are seen to rise sharply at high- p_T . This increase happens in either the bin $140 < p_T^{\tau_h} < 200$ GeV or $p_T^{\tau_h} > 200$ GeV. To map this effect, binned values are taken based off the algorithm shown in Figure 1.12 and the fit is used below the minimum bin.

The Landau and zeroth order polynomial fits are flattened at $p_T^{\tau_h}$ values where there is no significant downwards shift or at the final bin. Fake factor fits with respect to $p_T^{\tau_h}$ are shown in Figures 1.13-1.14. The fake factors are highest in the lowest

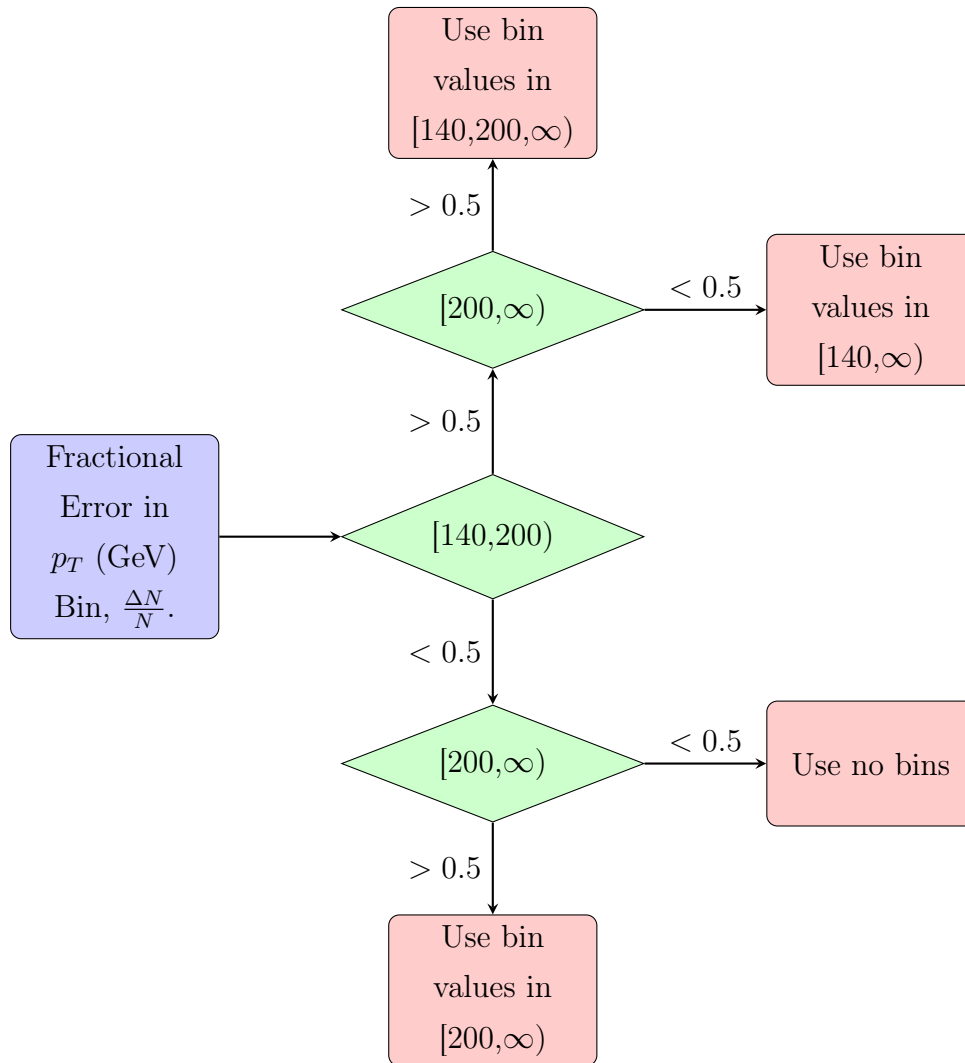


Figure 1.12: Flow chart of the algorithm used to determine where binned values are taken instead of the fit. The blue box represents the input, the green diamonds represent the decisions and the red boxes represent the outputs.

$p_T^{\text{jet}}/p_T^{\tau_h}$ bin and lowest in the highest $p_T^{\text{jet}}/p_T^{\tau_h}$ bin, as expected. Otherwise the fake factors fall with p_T in each category until the thresholds used for the high p_T binning algorithm.

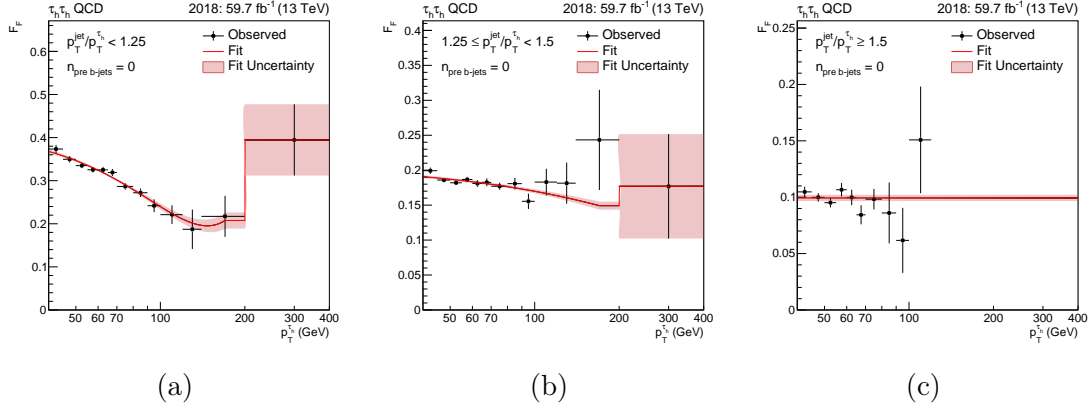


Figure 1.13: Fake factor fits in $\tau_h \tau_h$ channel for the QCD $N_{\text{pre b jets}} = 0$ category with 2018 data. The three jet p_T to $\tau_h p_T$ categories are shown.

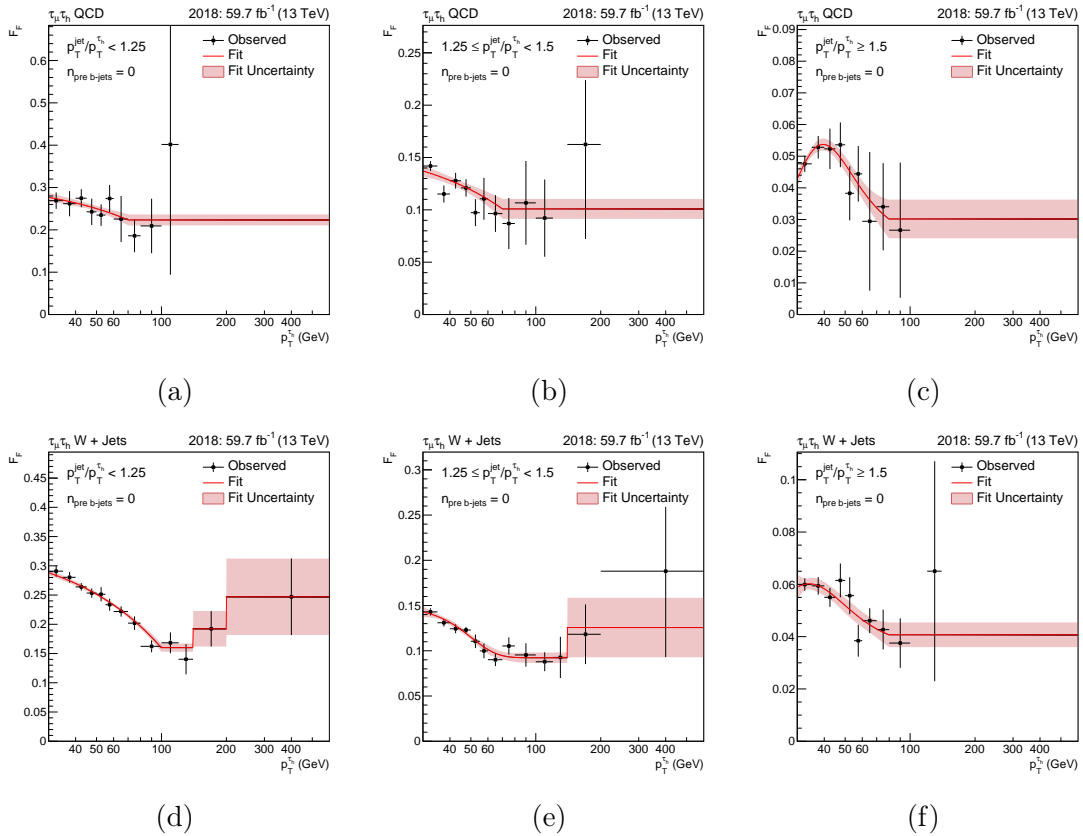


Figure 1.14: Fake factor fits in $\mu \tau_h$ channel for the QCD and $W + \text{Jets}$ $N_{\text{pre b jets}} = 0$ category with 2018 data. The three jet p_T to $\tau_h p_T$ categories are shown for each process.

1.7.3 Corrections

In the $\tau_h\tau_h$ channel, the measured F_F^{QCD} are then corrected to account for non-closures in other variable in the **Determination Region**. The only significance non-closures are observed for E_T^{miss} related variables and are largest for events with $N_{\text{pre b jets}} = 0$. Closure corrections are performed for the variable ΔR in bins of $N_{\text{b jets}}$. In the $\mu\tau_h$ and $e\tau_h$ channels, the measured F_F^{QCD} and $F_F^{\text{W+jets}}$ are corrected for non-closures observed in the E_T^{miss} variables and $p_T^{e/\mu}$ distributions. A study was performed to determine the nature of these non-closures and it was found that the cause was due to fake E_T^{miss} arising from mismeasurement of the energies of particles in a jet. A diagram of this effect is shown in Figure 1.15.

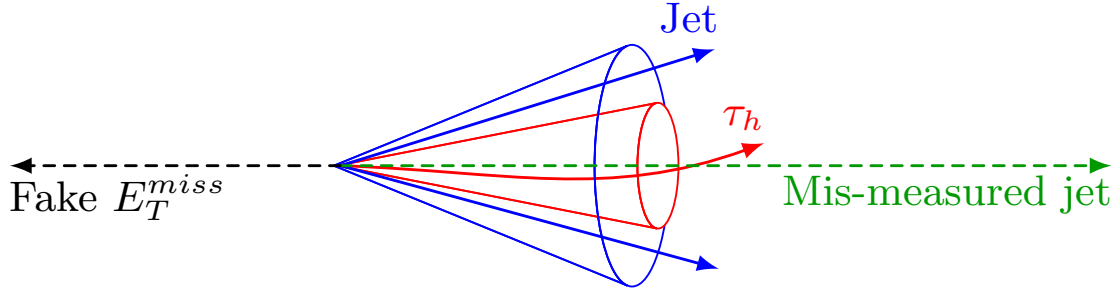


Figure 1.15: Diagram showing how fake E_T^{miss} arises from mismodelling jet constituents in τ_h identification.

To correct for this effect, the QCD fake factors are corrected as a function of C_{QCD} , where C_{QCD} is defined as,

$$C_{\text{QCD}} = \frac{E_T^{\text{miss}} \cos \Delta\phi(\vec{p}_T^{\text{miss}}, \vec{p}_T^{\tau_h})}{p_T^{\tau_h}}. \quad (1.6)$$

where $\Delta\phi(\vec{p}_T^{\text{miss}}, \vec{p}_T^{\tau_h})$ is the separation in the azimuthal angle between the the missing a \vec{p}_T^{miss} and $\vec{p}_T^{\tau_h}$. The numerator quantifies the missing transverse momentum in the direction of the τ_h candidate. Once divided by the τ_h p_T , C_{QCD} is a measure of the fraction of missing to visible τ_h transverse momentum aligned with the τ_h . For $W + \text{jets}$ and $t\bar{t}$ the situation is slightly different due to the presence of genuine missing energy from neutrinos. In this case, the correction variable is modified to approximately subtract the genuine E_T^{miss} from the total. This approximation assumes the neutrino is back-to-back and balanced with the light lepton (which is

exactly true for W bosons produce at rest in the transverse direction). The equation then becomes,

$$C_W = \frac{(E_T^{\text{miss}} + p_T^{e/\mu}) \cos \Delta\phi(\vec{p}_T^{\text{miss}} + \vec{p}_T^{e/\mu}, \vec{p}_T^{\tau_h})}{p_T^{\tau_h}}. \quad (1.7)$$

When either correction variable is separated from 0, a larger quantity of fake E_T^{miss} is expected in the event. In these regions a large correction is needed due to the mis-measured jet energy spectrum shifting the τ_h candidate isolation and so shifting the τ identification scores. Examples of these closure corrections are shown in Figure 1.16

After the **Determination Region** is modelled well for all variables of interest, extrapolation corrections from the fake factors derived in B applied to region D are calculated. In the $\tau_h\tau_h$ the correction is parameterised by the p_T of the leading τ_h candidate, in the $e\tau_h$ and $\mu\tau_h$ channels it is parameterised by the p_T of the light lepton. Where statistics allow, these corrections are calculated in the high mass optimisation procedure categories. Examples of the extrapolation corrections are shown in Figure 1.17.

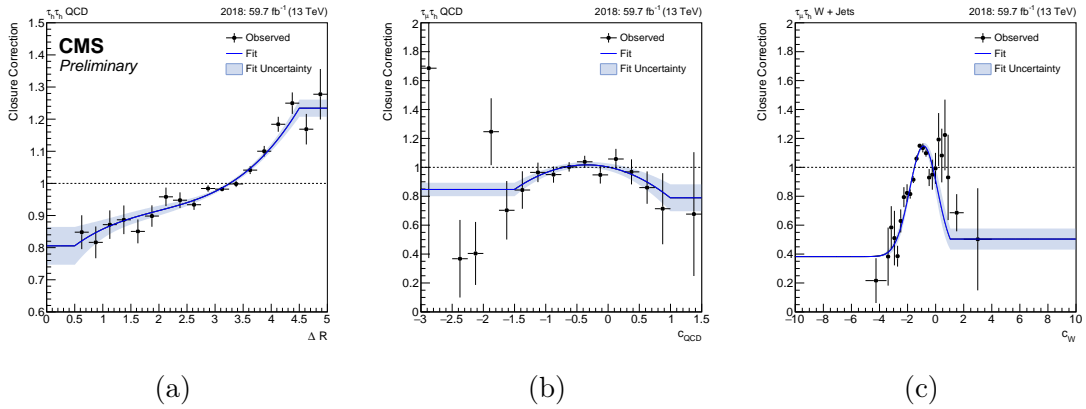


Figure 1.16: Determination region closure correction fits with 2018 data. (a) is the correction parametrised by ΔR in events with $N_{b \text{ jets}} = 0$ in the $\tau_h\tau_h$ channel. (b) and (c) show the correction for the $\mu\tau_h$ channel parametrised by the specific correction variables defined in Equation 1.6 and 1.7 for QCD and W + jets processes respectively.

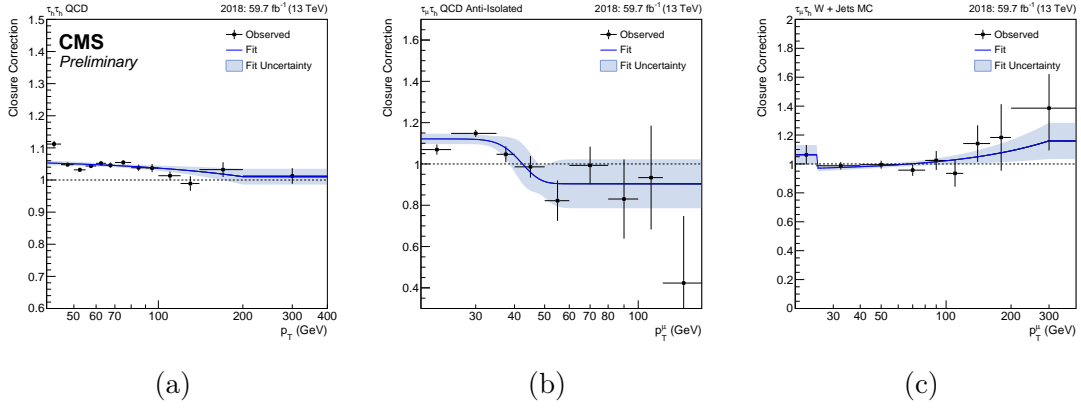


Figure 1.17: Determination region to application region closure correction fits with 2018 data. (a) is the correction moving from same sign to opposite sign τ leptons the parameterised by leading $\tau_h p_T$ in events with $N_{\text{b-jets}} = 0$ in the $\tau_h\tau_h$ channel. (b) and (c) show the correction for the $\mu\tau_h$ channel moving from same sign to opposite sign τ leptons and high m_T to low m_T both parameterised by the the muon p_T for QCD and W + jets processes respectively.

1.7.4 Applying Fake Factors

In the $e\tau_h$ and $\mu\tau_h$ channels the F_F^i measured for the different processes are combined into an overall factor, F_F , using

$$F_F = \sum_i f_i \cdot F_F^i, \quad (1.8)$$

where the factor f_i is defined as

$$f_i = \frac{N_{\text{AR}}^i}{\sum_j N_{\text{AR}}^j}, \quad (1.9)$$

which is the fraction of events with a jet $\rightarrow \tau_h$ originating from process i over the total number of jet $\rightarrow \tau_h$ events for all processes in the application region. These fraction of events are estimated with MC, with a QCD model extrapolated from same sign τ pairs. It is observed that W + jets is the dominating process in this region, however, there are affects from QCD at low m_T and from $t\bar{t}$ in the b tagged categories. These fractions are then multiplied to the relevant corrected fake factor and applied to the fail region in C, with any events which are not jet $\rightarrow \tau_h$ subtracted off with MC.

For the $\tau_h\tau_h$ channel there are two τ_h candidates that a jet can be misidentified as. For this analysis, the fake factors are only applied the leading τ_h candidate failing

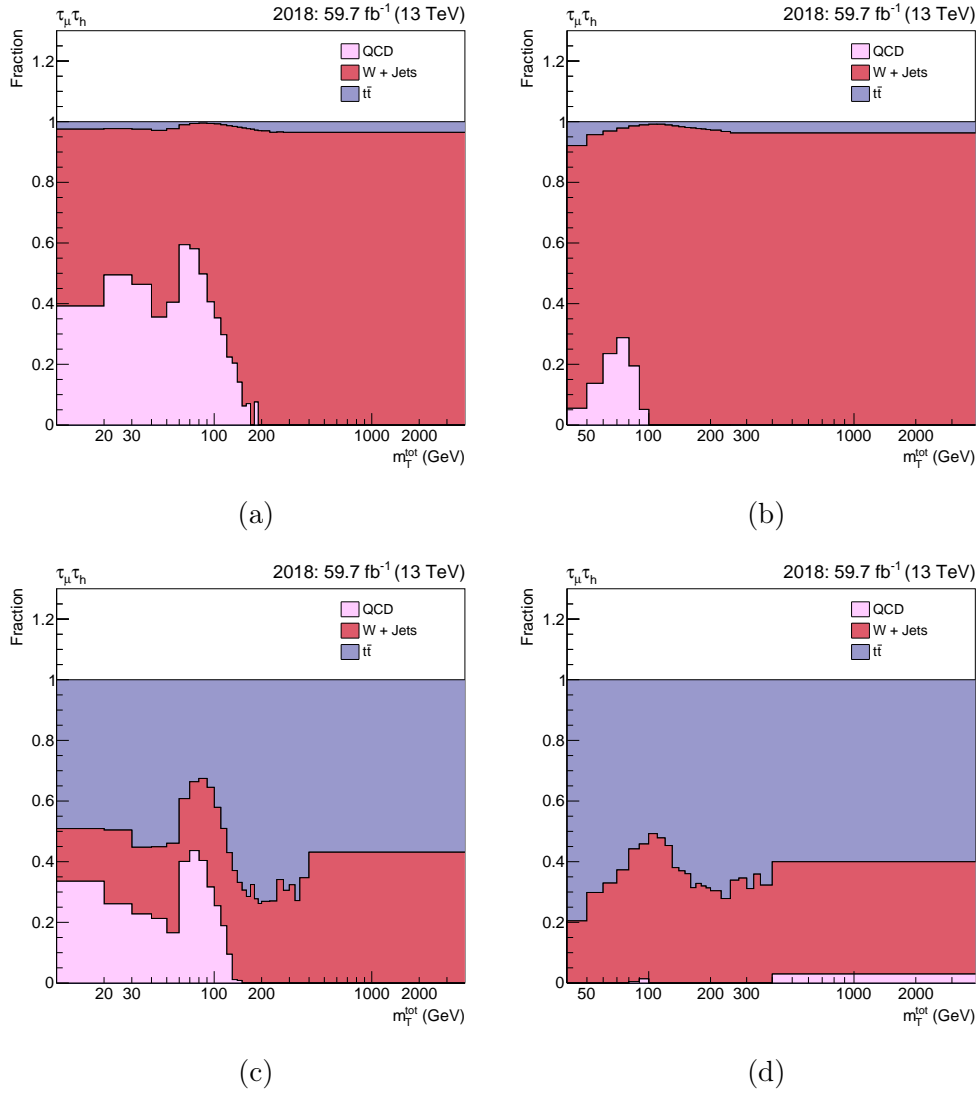


Figure 1.18: The expected application region fractions of the processes in the $\mu\tau_h$ channel. (a) and (b) show the no b tag Tight- m_T and Loose- m_T categories and (c) and (d) show the b tag Tight- m_T and Loose- m_T categories respectively.

the τ_h ID in C. This models all events where the leading τ_h candidate is a jet $\rightarrow \tau_h$. However, this leaves a small fraction of events, where the leading candidate is a genuine τ and the sub-leading candidate is a jet $\rightarrow \tau_h$. This contribution (mostly from $W + \text{jets}$) is added back with MC.

1.8 MC Corrections

The corrections apply both to simulated and embedding samples as the τ decay is simulated, however they are derived separately. For electrons and muons, corrections are applied to triggers, tracking efficiencies, and the identification and isolation requirements. Using the ‘tag-and-probe’ method, they are obtained in bins of p_T and η of the corresponding lepton, with $Z \rightarrow ee$ and $Z \rightarrow \mu\mu$ events. These corrections are generally no more than a few percent. The electron energy scale is adjusted to the scale measured in data using the Z boson mass peak in $Z \rightarrow ee$ events.

Similarly, corrections are derived for the efficiency of triggering and identification efficiency of τ_h candidates. In the $e\tau_h$ and $\mu\tau_h$ channels, trigger efficiency corrections are obtained from the ratio of fits to data versus simulated samples, for the trigger efficiency as a function of p_T . For the $\tau_h\tau_h$ channel, this is instead done using the binned values of the τ_h decay modes. The identification efficiency corrections are derived as a function of the p_T of the τ_h candidate. Corrections to the energy scale of the τ_h candidates and of electrons misidentified as τ_h candidates are obtained from likelihood scans of discriminating observables, such as the reconstructed τ_h candidate mass. For muons misidentified as τ_h candidates, the energy scale correction is negligible.

The correction of the missing transverse energy’s magnitude and resolution in the embedding samples is needed to account for the incomplete removal of energy deposits from muons replaced by simulated τ decays during the embedding procedure. These corrections are derived by comparing p_T^{miss} in embedded events to fully simulated events.

In fully simulated events, a specific trigger inefficiency caused by a shift in the timing of the inputs of the ECAL L1 trigger in the region at $|\eta| > 2.0$ during the 2016 and 2017 data taking. This effect is named pre-firing. This resulted in a loss of efficiency for events containing an electron or jet with p_T larger than ≈ 50 or ≈ 100)

GeV respectively, in the region of $2.5 < |\eta| < 3.0$. Corresponding corrections are derived from data and applied to the simulation.

Corrections on the energy of jets are calculated in bins of the jet p_T and η . These range from subpercent levels in the central part of the detector to a few percent in the forward region. The energy resolution of the simulated jets is also tuned to match that of the data. A correction is applied to the missing transverse momentum, based on differences in the estimated hadronic recoil between data and simulation. A MC to data correction for a b jet to pass the selection criteria is also determined. These corrections can adjust the number of b jets in a simulated event.

Any differences from simulated events to data, where an electron or muon is reconstructed as a τ_h , are corrected from the pure $Z \rightarrow ee$ and $Z \rightarrow \mu\mu$ regions. Similarly, a correction is applied to account for residual differences in the $\mu \rightarrow e$ misidentification rate between data and simulation.

Further MC to data corrections are applied to the dilepton mass and p_T spectra in simulated $Z \rightarrow ll$ events. These are derived from $Z \rightarrow \mu\mu$ events. Additionally, all simulated $t\bar{t}$ events are weighted to match the top quark $p_T t$ distribution observed in data.

1.9 Uncertainty Model

The statistical uncertainties are taken into account by the Barlow-Beeston method, described in Ref. [30, 31]. The systematic model is split into uncertainties based on the online and offline reconstruction of objects and the background and signal modelling. An uncertainty is correlated across channels when it represents a shift on the reconstruction of an object and decorrelated otherwise. It is decorrelated across era of data taking when the shift is derived independently by era. The embedded samples use the same uncertainty scheme as MC but 50% are correlated and 50% uncorrelated with MC uncertainties, because of the shared real data in the measurement.

Hadronic Taus

Uncertainties on the τ_h triggers are obtained from the fitted scale factors used to derive the corrections for the τ_h trigger efficiencies. The legs of the double- τ_h and e/μ - τ_h cross triggers in different decay mode bins are treated as uncorrelated. For the single- τ_h trigger leg, due to limited statistics it is not possible to determine scale factors and uncertainties split by decay mode and therefore a single uncertainty common to all decay modes is applied. The double- τ_h trigger uncertainties are further split in the p_T regions < 100 GeV and > 100 GeV to allow the fit more freedom to adjust the high p_T regions relative to the low p_T regions. Uncertainties are also applied on the energy scale of the τ_h candidates. These uncertainties range between 0.2 and 1.1%. Finally, an uncertainty on the ID efficiency is placed as a function of p_T in the $e\tau_h$ and $\mu\tau_h$ channels, and of the τ_h decay mode in the $\tau_h\tau_h$ channels. These vary between 3-9% and is uncorrelated in each variable bin it is derived in. To account for the different anti-lepton discriminator working points, an uncertainty of 3% per τ_h is applied and treated as uncorrelated between the channels where different $D_{\text{WP}}^{e/\mu}$ are used.

Light leptons

The uncertainty on the trigger efficiencies amounts to 2% per lepton in the $e\tau_h$, $\mu\tau_h$ and $e\mu$ channels. They are basically normalisation uncertainties but implemented as shape uncertainties as they only touch the events triggered by the corresponding cross trigger or single lepton triggers. Uncertainties are also placed on the electron energy scale based off the calibration of ECAL crystals. This information is not reliable for embedding samples and so uncertainties of 0.5-1.25% are placed here. The energy scale variations are negligible and so not included. Another 2% uncertainty is placed on the ID of any electron or muon in the event.

Jets

Jet energy scale and resolution uncertainties arise from a number of sources. These include limited statistical measurements used for calibration, energy measurement changes due to detector ageing, and bias corrections to address differences between simulation and data. Uncertainty ranges are from sub-percent to $\mathcal{O}(10\%)$. Uncertainties are also placed on the tagging of b jets, which vary from 0-3%.

Leptons misidentified as hadronic taus

Uncertainty shifts are applied for the energy scale of leptons faking τ_h parametrised by the p_T of the $e/\mu \rightarrow \tau_h$ fake. The magnitude is 1.0% for muons in all eras and for electrons the uncertainties vary between 0.5 and 6.6 %.

Jets misidentified as hadronic taus

The backgrounds with jets misidentified as τ_h are estimated from data with the fake factor method. There are different sources of uncertainty related to this method. The first uncertainties come from subtracting off other background processes with MC to form the determination region. The subtraction is shifted up and down by 10% to determine new weights. Next, statistical uncertainties on all of the fake factor method fits are accounted for, where the binned values are uncorrelated with the rest of the fit. An uncertainty is also placed on the choice of fit function, the shifts are estimated by comparing the fits to a 1st order polynomial fit set to constant above 100 GeV. The final systematic variation are then on the extrapolation corrections by applying the corrections twice and not at all. The size of each systematic uncertainty varies from 0–10%, whilst the statistical element from the fits can be larger in the tails of the distributions.

Jets misidentified as light leptons

Background with jets misidentified as electrons or muons from QCD are only considered in the $e\mu$ channel and modelled from data. Uncertainties are placed based on the statistical uncertainties in the determination region which are 2–4% and the extrapolation to the signal region that are $\mathcal{O}(10\%)$.

Muons misidentified as electrons

Background with muons misidentified as electrons are only considered in the $e\mu$ channel. These events are modelled from MC and any generator matched muon identified as an electron are given a 15%–45% uncertainty, that is derived from the initial corrections.

MET

The MET uncertainties is different dependent on process. For all processes that are not $t\bar{t}$ and diboson, the hadronic recoil response and its resolution are varied within

the uncertainties determined during the computation of the recoil corrections. For $t\bar{t}$ and diboson an uncertainty is derived on the energy carried by an unclustered particle [32]. These uncertainties vary between 0–10%.

Background process specific uncertainties

Uncertainties on the $t\bar{t}$ p_T and DY m_{ll} - p_T reweighting is placed by the applying the correction twice and not at all. An additional uncertainty is placed to cover the $t\bar{t}$ contamination in embedding, where the removed $t\bar{t}$ genuine τ pair is shifted up and down by 10%. Some non-closures are observed in embedded $Z \rightarrow \mu\mu$ control samples. Therefore, these non-closures are taken as an additional shape uncertainty as a function of the Z p_T and $m_{\tau\tau}$. Uncertainties on the normalisation background processes with sizes 4% for $Z \rightarrow ll$ and $W + \text{jets}$ production [25], 6% for $t\bar{t}$ production [26, 27], and 5% for diboson and single t quark production [27, 28, 29].

Signal process specific uncertainties

For the $g\bar{g}\phi$ process, in particular for low mass hypotheses, the variation of **hdamp** parameter of the POWHEG MC generator as well as the μ_R/μ_F scale variations are used to determine the uncertainties on the p_T spectrum of each contribution at NLO QCD to the Higgs boson production via gluon fusion (top, bottom, top-bottom interference). These are also determine from additional samples produced up to the generator level, and applied as event weights dependent on generator level p_T after the parton shower simulation. These uncertainties are included as shape uncertainties as they may affect the shapes of the m_T^{tot} distribution as well as the predicted signal yields.

Luminosity

(1.2 %, 2.3 %, 2.5 %) normalisation luminosity uncertainty is applied to the (2016, 2017, 2018) templates which originate from MC simulation.

Prefiring

Upper and lower bounds are taken from the efficiency maps and propagated on all MC samples as shape uncertainty for 2016 and 2017. The size of the uncertainty as the weight itself depends on the event topology. In general the uncertainty is at the order of 1%.

1.10 Signal Extraction

A simultaneous binned maximum likelihood fit over all analysis categories is used to extract the results. The likelihood takes the form,

$$\mathcal{L}(\text{data} \mid \mu, \theta) = \prod_i^{N_i} \text{Poisson}\left(n_i \mid \sum_j^{N_j} g_j(\mu_{ij}) \cdot s_{ij}(\theta) + \sum_k^{N_k} b_{ik}(\theta)\right) \cdot p(\hat{\theta} \mid \theta), \quad (1.10)$$

where i loops through all histogram bins and analysis categories. The indices j and k loop over all signal and background processes for the hypothesis being fit. n_i , s_i and b_i are the data observed, signal and background expectation respectively in each bin. θ represents the set of nuisance parameters (corresponding to the systematic uncertainties as detailed in Section 1.9) that parametrise the signal and background modelling. μ are rate parameters and $g(\mu)$ are scaling functions that scale to a signal to a specific hypothesis. The form of the Poisson probabilities are,

$$\text{Poisson}(n \mid x) = \frac{x^n e^{-x}}{n!}. \quad (1.11)$$

Finally, $p(\hat{\theta} \mid \theta)$ represents the probability density function (pdf) of each nuisance parameter (θ) with respect to the initial value of the parameter ($\hat{\theta}$).

The pdfs come in two forms, the first is for uncertainties that only affect the normalisation of the process and are modelled by log-normal pdfs. The second is for uncertainties that affect the shape of the distribution, these are assigned Gaussian pdfs. The $\pm 1\sigma$ shifts for each shape variations are derived and vertical morphing [31] is used to interpolate and extrapolate within and outside the shifts. Both pdfs are dependent on the mean (μ) and standard deviations (σ) and the functional forms are shown in Table 1.3.

Gaussian	Log-normal
$f(x) = \frac{1}{\sqrt{2\pi\sigma^2}} \exp\left(-\frac{(x-\mu)^2}{2\sigma^2}\right)$	$f(x) = \frac{1}{x} \frac{1}{\sqrt{2\pi\sigma^2}} \exp\left(-\frac{(\ln x - \mu)^2}{2\sigma^2}\right)$

Table 1.3: pdfs used for nuisance parameters.

The following subsections discuss the results of many such fits. The key fits to understand the results are the background-only fit and the signal-plus-background fits.

The background-only fit is performed with N_j (number of signal processes) set to 0. For all signal-plus-background fits, the fit is done with respect to a single mass hypothesis, however within this mass hypothesis can be a number of signal processes. The model independent resonance search has separate $gg\phi$ and $bb\phi$ signal modes and so two rate parameters $\mu_{gg\phi}$ and $\mu_{bb\phi}$ are needed. When the samples are initially scaled to the cross section times branching ratio ($\sigma \times B(\phi \rightarrow \tau\tau)$) of 1 pb and $g(\mu) = \mu$ for both processes, $\mu_{gg\phi}$ and $\mu_{bb\phi}$ represent the $\sigma \times B(\phi \rightarrow \tau\tau)$ with units of pb. To avoid negative signal strengths, μ will only be taken to be positive. Also used in the following subsections, is a signal-plus-background channel/category compatibility fit. In this fit the signal processes and rate parameters are further split in each channel or category utilising index i in Eq. 1.10. This is used to determine the compatibility of the results in different decay channels and analysis categories. In this case, μ is allowed to take negative values to help fully understand the fits to data in each channel or category.

The vector leptoquark search has two signal modes; the t-channel interaction and the interference with Drell-Yan. However, as this is a model-dependent interpretation of these results both these rate parameters scale together. The scaling functions differ between the two processes with $g_{\text{t-channel}}(\mu) = \mu^4$ and $g_{\text{interference}}(\mu) = \mu^2$ to mimic how the cross sections of each process scales. When the initial samples are scaled to cross section at $g_U = 1$, μ corresponds to the coupling g_U .

For the MSSM interpretation of the results, there are three Higgs bosons to consider in the signal model (h, H and A) produced via both gluon fusion and in association with b quarks. The $gg\phi$ samples are also split into the separate loop contributors, so the kinematic properties can be properly scaled to MSSM prediction, as described in Section 1.1.1. The SM-like Higgs boson is considered in the MSSM signal model to monitor differences in the observed Higgs boson prediction between the MSSM and the SM. In each benchmark scenario chosen, the signal prediction depends only on m_A and $\tan\beta$ and the scaling to cross section is shown in Eq. 1.1. As the potential scaling functions for MSSM interpretations are not necessarily smooth one-to-one mappings, the likelihood is tested for individual points on the m_A - $\tan\beta$ parameter space. At each point, the MSSM Higgs bosons are scaled to the theory predicted cross section times branching ratio. To test the MSSM hypothesis over the SM hypothesis, the single rate parameter μ is used and only allowed to take values of 1 (MSSM) and 0 (SM) with $g(\mu) = \mu$. As the SM Higgs boson is added to the

background modelling and the MSSM prediction of the observed Higgs boson is added to the signal model when $\mu = 1$, the SM Higgs boson prediction must then be subtracted from the signal model.

The confidence intervals in the best fit results are given by the $-2\Delta \ln \mathcal{L}$, where $\Delta \ln \mathcal{L}$ is the difference between $\ln \mathcal{L}$ of the best fit model and the test value of μ . The 68% and 95% confidence regions with two degrees of freedom (as in the model independent resonant search) are determined by $-2\Delta \ln \mathcal{L} = 2.28$ and 5.99 respectively.

Upper limits are placed using the modified frequentest approach [33, 34] with a profile likelihood ratio used for the test statistic, as defined below.

$$q_\mu = -2 \ln \left(\frac{\mathcal{L}(\text{data} | \mu, \hat{\theta}_\mu)}{\mathcal{L}(\text{data} | \hat{\mu}, \hat{\theta}_{\hat{\mu}})} \right), 0 \leq \hat{\mu} \leq \mu, \quad (1.12)$$

where $\hat{\mu}$ and $\hat{\theta}_{\hat{\mu}}$ are the best fit values of μ and θ . $\hat{\theta}_\mu$ are the values of θ that is maximised by the likelihood for a tested value of μ . The bounds on $\hat{\mu}$ are to ensure a positive signal strength with a one-sided confidence interval. The probability of $q_\mu \geq q_\mu^{\text{obs}}$ is,

$$\text{CL}(\mu) = \int_{q_\mu^{\text{obs}}}^{\infty} f(q_\mu | \mu, \theta_\mu^{\text{obs}}), \quad (1.13)$$

where $f(q_\mu | \mu, \theta_\mu^{\text{obs}})$ is the pdf of q_μ . CL_b and CL_{s+b} are then defined by the relevant background-only and signal-plus-background fits. CL_s is defined as the ratio of CL_{s+b} and CL_b and then upper limits are placed at the confidence level of $1 - \text{CL}_s$. The $f(q_\mu | \mu, \theta_\mu^{\text{obs}})$ are determined using the asymptotic approximation [35] and results are cross-checked and deemed consistent with toy MC datasets.

If a deviation from the background expectation is observed, the size of the deviation is quantified by a significance. To test rejection of the background-only hypothesis in favour of the signal-plus-background hypothesis, μ is replaced with 0 in the test statistic. The p -value, p_0 is then,

$$p_0 = \int_{q_0^{\text{obs}}}^{\infty} f(q_0 | 0, \theta_\mu^{\text{obs}}). \quad (1.14)$$

p_0 is uniformly distributed between 0 and 1 for the background-only hypothesis and so the probability and significance of rejecting the background-only hypothesis can be found.

1.11 Postfit Plots

Figures 1.19 and 1.20 show the unblinded distributions in the most sensitive analysis categories. For simplicity, the $e\tau_h$ and $\mu\tau_h$ channels have been combined. Figure 1.19 shows the distributions of the $m_{\tau\tau}$ discriminator in the no b tag low-mass optimisation categories. A signal-plus-background fit for a model-independent gluon fusion resonant mass hypothesis of 100 GeV is shown and the changes in the background modelling when using a background-only fit is displayed in the ratio. Figure 1.20 shows the distributions of the m_T^{tot} discriminator in the high mass optimisation categories. A background-only fit is shown for the stacked background and example signal hypotheses for the model independent 1.2 TeV $gg\phi$ and $bb\phi$ resonances and VLQ (BM 1) 1 TeV mass points are displayed.

In the low-mass optimisation categories, a small excess of events is observed on the Z boson peak in the no b tag categories and reasonable agreement is observed in the b tag categories. The excess of events are distributed in $m_{\tau\tau}$ between 80 and 120 GeV. A signal-plus-background hypothesis is best fit with a 100 GeV $gg\phi$ signal with a cross section times branching ratio of 5.8 pb. In this same fit the $bb\phi$ process is constrained by the b tag categories to give a signal yield of 0. A background-only fit is also performed on the data, it is observed that this can only partly explain the differences observed between background and data. Even after a background-only fit there is still an small excess of data events over the Z boson peak.

In the high-mass optimisation categories, another small excess is observed in high m_T^{tot} bins, particularly in the most sensitive no b tag categories. This excess is best fit by a model independent gluon fusion resonant mass at 1.2 TeV with a cross section times branching ratio of 3.1 fb. There are no considerable differences observed in background modelling between signal-plus-background and background-only fits. This is as the uncertainties in these bins are more statistically dominated and the majority of the systematic uncertainties are constrained in the bulk of the distribution. Good agreement is observed in the rest of the distribution. There is a very small deviation in the b tag categories, but as this can also be explained by a $gg\phi$ signal, the $bb\phi$ signal is heavily constrained and so largely does not contribute to the signal-plus-background fit of the excess. Similar to the $bb\phi$ signal, the VLQ BM 1 signal is constrained by the results in the b tag categories, leading to a small non-zero best fit signal strength, but cannot explain the excess in the no b tag categories.

1.12 Model Independent Results

1.12.1 Limits

95% CL limits are set on the assumption of absence of a signal for the search for a $gg\phi$ or $bb\phi$ resonance and shown in Figure 1.21. In each case, the other process is allowed to float freely in the fit. The excesses observed in the postfit distributions act to weaken the observed limit compared to the expected limit at 100 GeV and 1.2 TeV, as more data was observed than expected. For $gg\phi$ production the expected limits flatten under 100 GeV, due to difficulty of separating signal from the Z boson at this mass. Both sets of limits vary from $\mathcal{O}(10 \text{ pb})$ at 60 GeV to 0.3 fb at 3.5 TeV.

95% expected limits are drawn on the fit to each di- τ decay channel individually and are shown in Figure 1.22. This gives a measure of the sensitivity of each channel. In the high mass optimisation categories, the combined limit is heavily dominated by the $\tau_h\tau_h$ channel. This is mostly driven by branching fraction, as all channels in this mass range have similar signal separation ability. In the high mass optimisation categories, the combined limit is more a contribution of all channels. In the $\tau_h\tau_h$ channel in this region, the QCD multijet background is the largest fraction of any non $Z \rightarrow \tau\tau$ backgrounds in all channels and so the limit for this channel is weakened and the other channels contribute to the combined limit more. The high double- τ_h trigger p_T thresholds (chosen because of the QCD multijet background) also lowers the signal acceptance in the $\tau_h\tau_h$ channel.

A comparison of the limits are also made with the ATLAS experiment and in particular the results presented in Ref. [36]. This ATLAS search looks for the same signal but over a smaller mass range, from 200 GeV to 2.5 TeV. Plots showing the comparison of the expected and observed limits for $gg\phi$ and $bb\phi$ are shown in Figure 1.23. The expected limits from the CMS and ATLAS results are roughly compatible over the shared mass range, except at high mass where the extra statistics from the embedded $Z \rightarrow \tau\tau$ samples compared to MC allow for lower background uncertainties and hence a stronger limit. The ATLAS result observed no excess of events compatible with $gg\phi$ signal at 1.2 TeV, in fact a small deficit was observed. Also, ATLAS observed local excesses at 400 GeV of 2.2σ for $gg\phi$ and 2.7σ for $bb\phi$. None of these

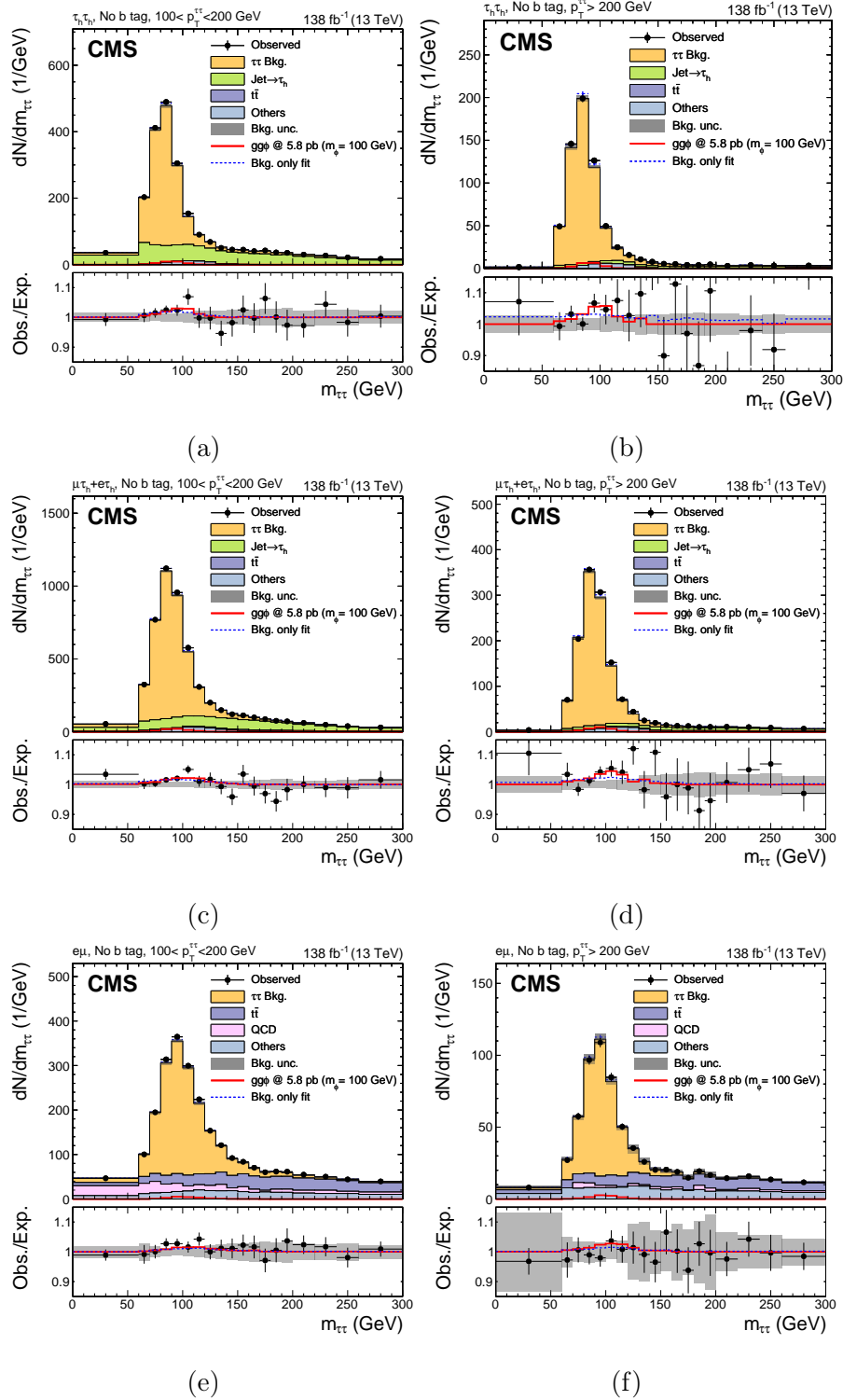


Figure 1.19: Distributions of $m_{\tau\tau}$ in the no b tag second highest (left) and highest (right) p_T category for the $\tau_h\tau_h$ (top), the combined $e\tau_h$ and $\mu\tau_h$ (middle) and the $e\mu$ (bottom) channels. The solid histograms show the stacked background predictions after a signal plus background fit to the data. The best fit gluon fusion signal for $m_\phi = 100$ GeV is shown by the red line. Also shown by a blue dashed line on the bottom pad is the ratio of the background predictions for the background only fit to the signal plus background fit

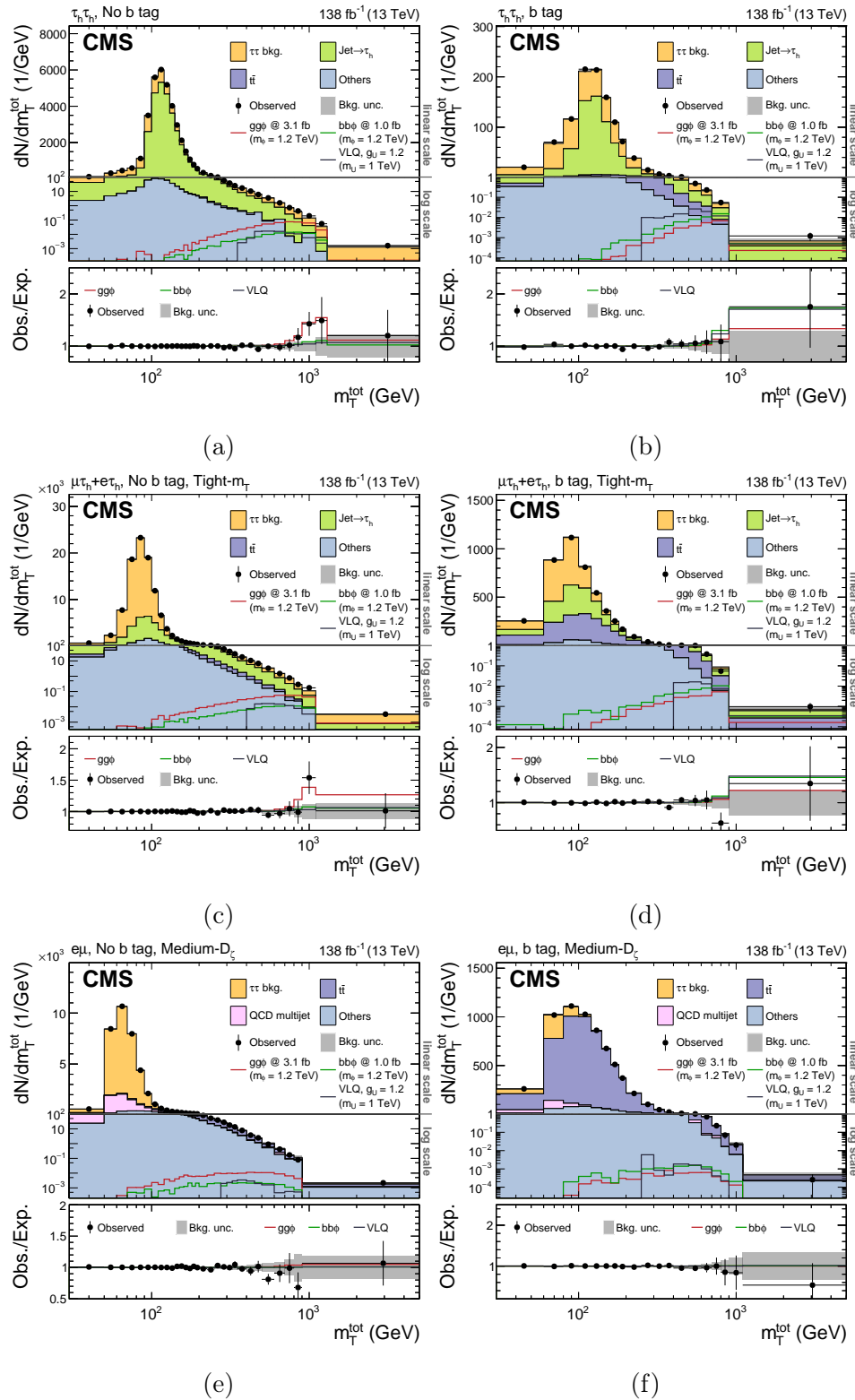
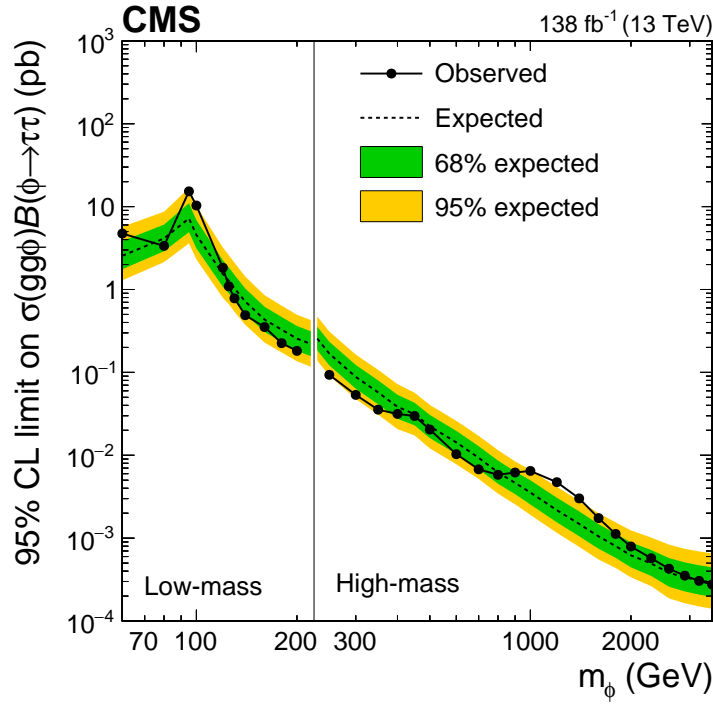
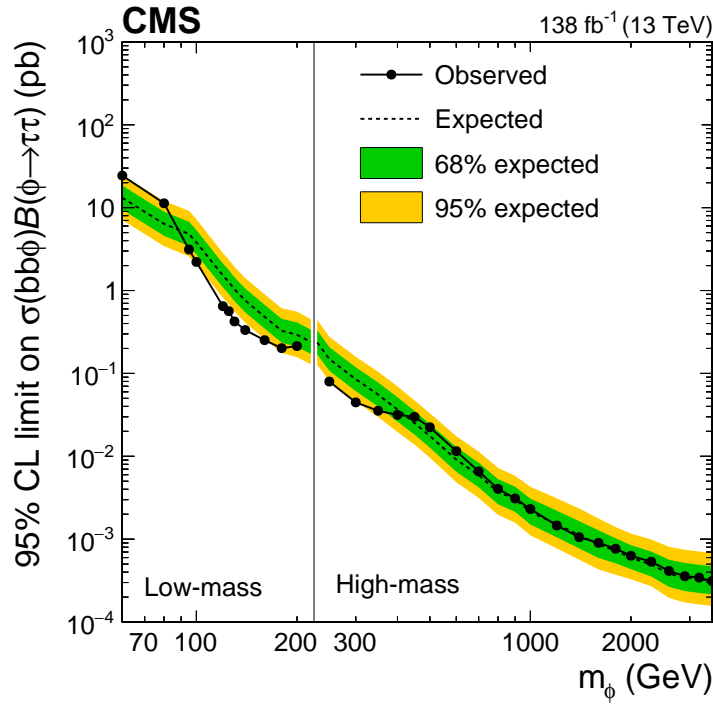


Figure 1.20: Distributions of m_T^{tot} in the $\tau_h \tau_h$ no b tag (a) and b tag (b) categories, the combined $e \tau_h$ and $\mu \tau_h$ no b tag (c) and b tag (d) Tight- m_T categories and the $e \mu$ no b tag (e) and b tag (f) Medium- D_ζ categories. The solid histograms show the stacked background predictions after a background only fit to the data. The best fit gluon fusion signal for $m_\phi = 1.2$ TeV is shown by the red line, b associated production and U_1 signals are also shown for illustrative purposes.



(a)



(b)

Figure 1.21: Expected (dashed line) and observed (solid line and dots) 95% CL upper limits on the product of the cross sections and branching fraction for the decay into τ leptons for (a) $gg\phi$ and (b) $bb\phi$ production in a mass range of $60 \leq m_\phi \leq 3500$ GeV. The dark green and bright yellow bands indicate the central 68% and 95% intervals for the expected exclusion limit.

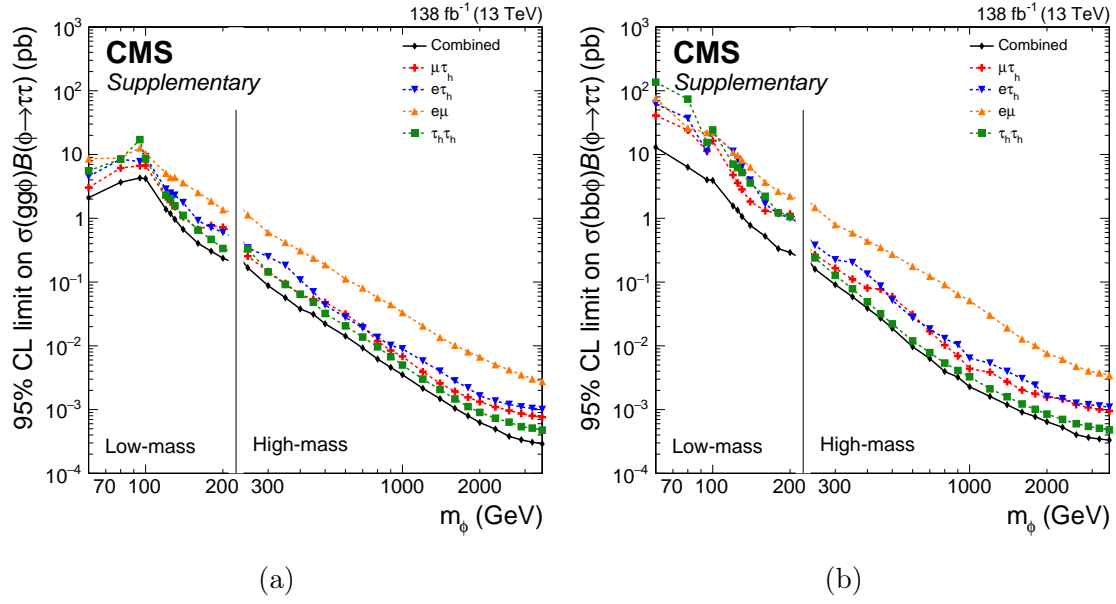


Figure 1.22: Comparison of the expected 95% CL upper limits on the product of the cross sections and branching fraction for the decay into τ leptons for (a) $gg\phi$ and (b) $bb\phi$ production, split by the $\tau\tau$ decay products fit individually.

excesses are consistent between the ATLAS and CMS results. The ATLAS search does not stretch to the mass of the low mass CMS excess and so cannot be used a cross-check for this.

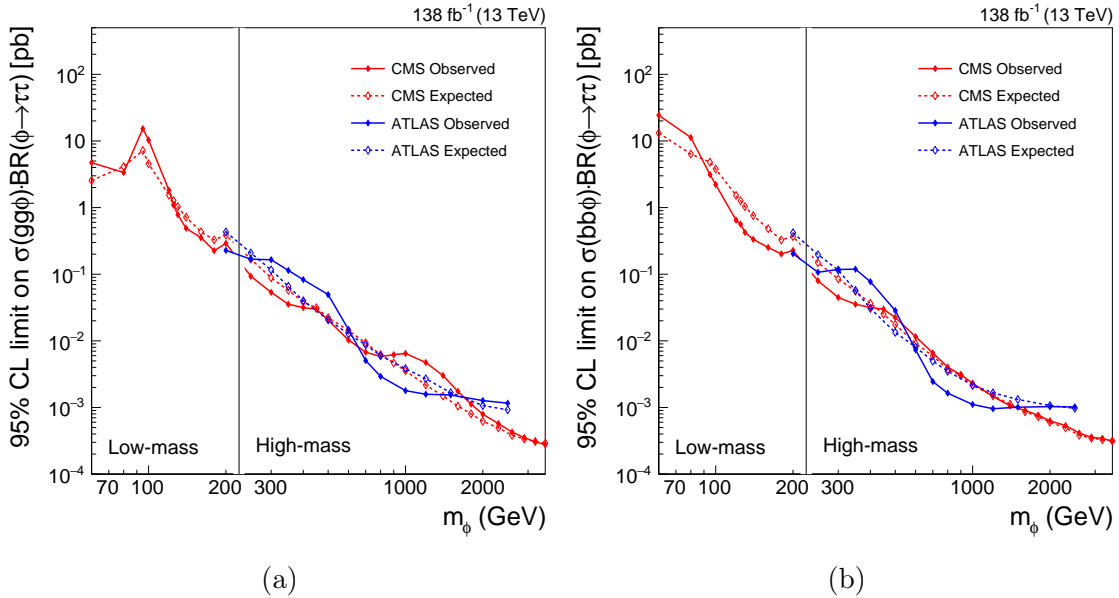


Figure 1.23: Comparison of the expected 95% CL upper limits on the product of the cross sections and branching fraction for the decay into τ leptons for (a) $gg\phi$ and (b) $bb\phi$ production, split by the CMS result detailed in this thesis and the ATLAS result from Ref. [36].

1.12.2 Significance and Compatibility

The p -values and significances at each model independent signal hypothesis are calculated as described in Section 1.10 and shown in Figure 1.24. Identical to the model independent limits, the $gg\phi$ or $bb\phi$ process is allowed to float freely if not the parameter of interest. The excesses for the $gg\phi$ process peak at 100 GeV and 1.2 TeV and quantify to a local (global) significance of 3.1σ (2.7σ) and 2.8σ (2.2σ) respectively. There are also excesses at neighbouring mass points (particularly at high mass), however this is consistent with the mass resolution of the fitted templates for the central values. No deviations beyond 2σ are observed for $bb\phi$ production.

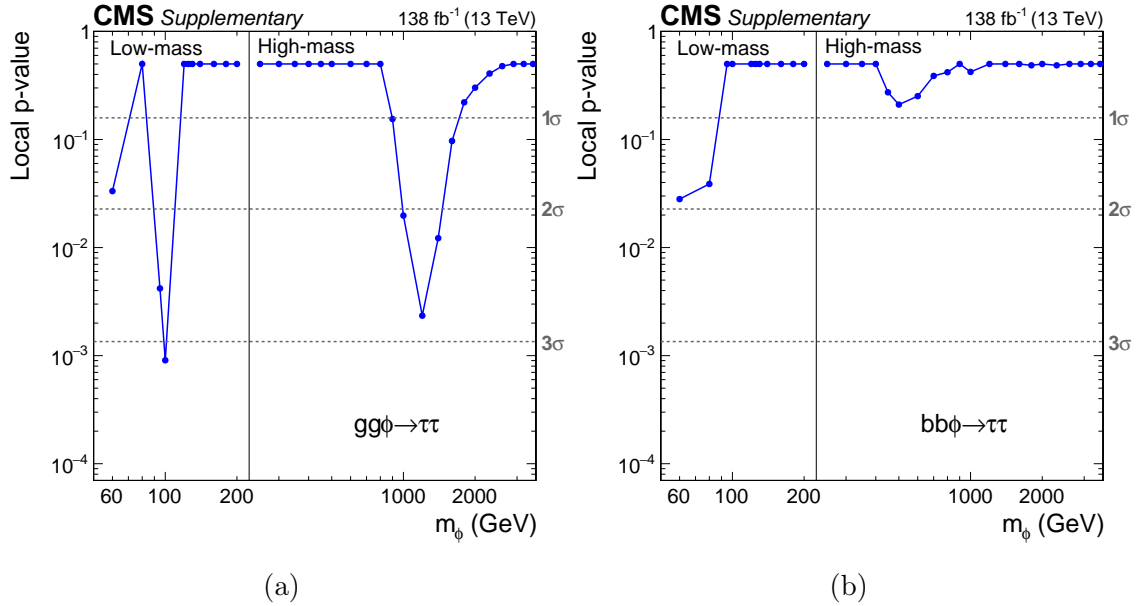


Figure 1.24: Local p -value and significance of a $gg\phi$ (left) and $bb\phi$ (right) signal as a function of m_ϕ .

As many different decay channels and categories are used to extract these significances, the signal strength is studied in each channel and category. This is done via compatibility fits as described in Section 1.10, where the signal strength parameter in each channel/category is decoupled. No statistically significant differences are observed in the best fit signal strength in any decay channel or category fit and p -values between each channel or category fit are always above 0.05. Figure 1.25 shows the results of the compatibility fits in the low-mass optimisation categories split by di- τ decay channels and the p_T bins fit. Figure 1.26 shows the compatibility fits in the high-mass optimisation categories split by di- τ decay channels. The low-mass signal strengths are no more dominant in any p_T region than another. In both low-

and high-mass cases, the signal strengths are consistent across di- τ decay channels. There is a small shift in the high mass $e\mu$ categories to a negative signal strength, these categories have little to no sensitivity to this signal in comparison to others and a small deficit is observed in data, resulting in fits for a negative signal strength with a large uncertainty.

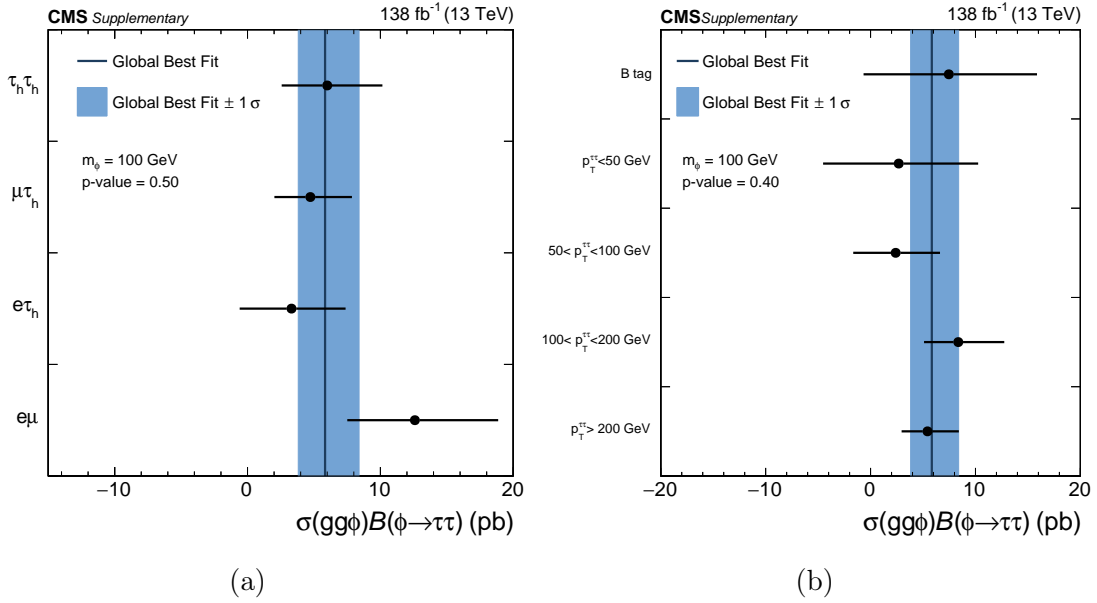


Figure 1.25: Compatibility plots of the 100 GeV excess split into analysis channels (a) and categories (b). In each case the fitted signal strength is decoupled in the bin shown on the plot.

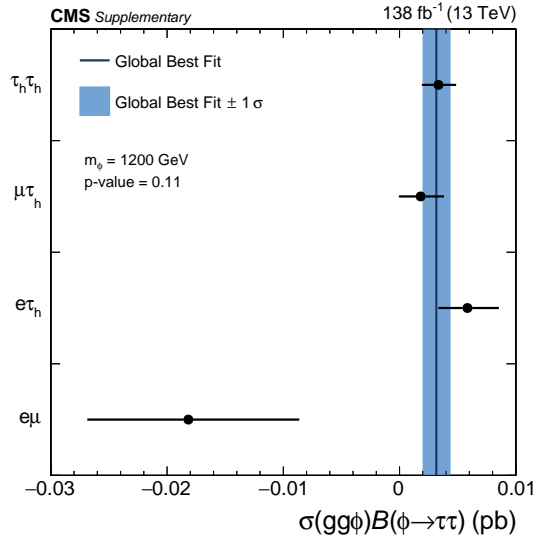


Figure 1.26: Compatibility plots of the 1.2 TeV excess split by analysis channels. In each case the fitted signal strength is decoupled in each channel.

1.12.3 2D Likelihood Scans

As the model-independent search looks for two signal modes at each mass point, the results for both processes happening simultaneously are studied. This is done in the form of 2D likelihood scans. The best fit cross section times branching fractions of each process and the 95% and 68% confidence intervals are shown for a number of different mass scenarios in Figure 1.27. The SM prediction in all plots is at (0,0). These results highlight how the excesses at 100 GeV and 1.2 TeV are dominated in the phase space in which $gg\phi$ and not $bb\phi$ signals are allowed. In the 60 GeV example, there are smaller deviations in both $gg\phi$ and $bb\phi$ and the SM background is again over 2σ away. Otherwise, signal strengths are completely compatible with the background expectation.

1.13 Model Dependent Limits

The exclusion contours for two benchmark scenarios of the MSSM, M_h^{125} and $M_{h,EFT}^{125}$, are presented in Figure 1.28. The red hatched regions denote areas where m_h is inconsistent with the observed SM Higgs boson mass within a ± 3 GeV boundary. For low values of $\tan\beta$, higher values of the additional SUSY particle masses, denoted as m_{SUSY} , are needed to explain a mass of approximately 125 GeV for the Higgs boson. In the M_h^{125} scenario, m_{SUSY} is fixed, and the predicted value of m_h is below 122 GeV. In contrast, the $M_{h,EFT}^{125}$ scenario adjusts m_{SUSY} to satisfy the required value of m_h for each point in $(m_A, \tan\beta)$ individually, accounting for the logarithmic corrections associated with the large values of m_{SUSY} using an effective field theory approach. The red hatched region in Figure 1.28 (b) indicates that the required values of m_{SUSY} exceed the GUT scale at very low values of m_A in this scenario. The Higgs boson masses, mixing angle α , and effective Yukawa couplings were calculated using FEYNHIGGS, and branching fractions for the decay into τ leptons and other final states were obtained from a combination of the FEYNHIGGS and HDECAY, following the prescriptions in Refs.[37, 38, 39], for the scenarios described in Ref.[4].

For the $M_{h,EFT}^{125}$ scenario, the sensitivity sharply drops at $m_A = 2m_t$ due to a drop in the branching fractions for the decay of A and H into τ leptons, when the A and H decays into two on-shell top quarks becomes kinematically accessible. Both scenarios are excluded at 95% CL for $m_A \lesssim 350$ GeV. For $m_A \lesssim 250$ GeV, most of the ggH/A events do not enter the no b tag categories due to the $m_{\tau\tau} > 250$ GeV

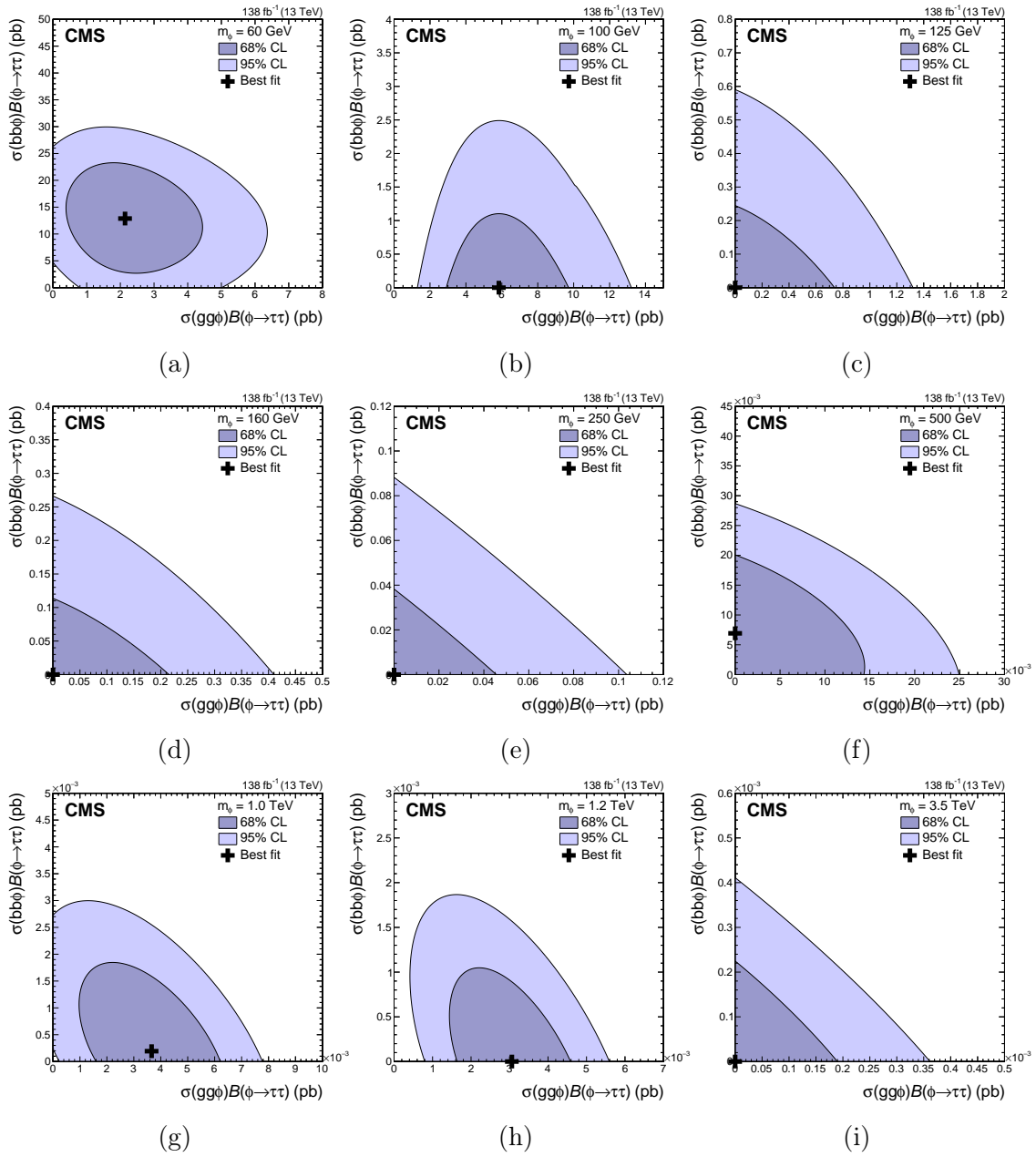


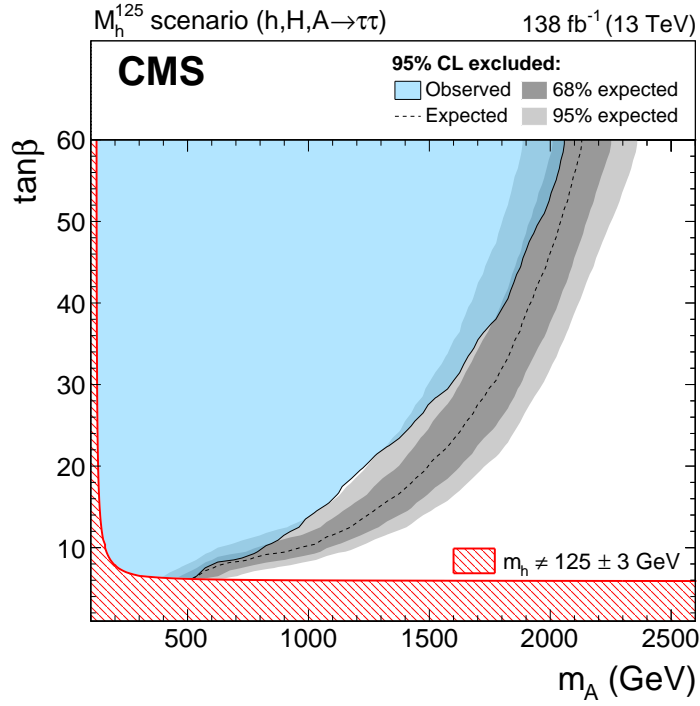
Figure 1.27: Maximum likelihood scans, including 68% and 95% CL contours obtained from the signal likelihood for the model-independent search. The scans are shown for selected values of m_ϕ between 60 GeV and 3.5 TeV.

requirement. In this parameter space, the sensitivity to the MSSM is driven by the measurements of the observed Higgs boson, even though H and A still contribute to the categories here. The sensitivity to the H and A enters mainly via the $bb\phi$ signal in the b tag categories, especially for increasing values of $\tan\beta$.

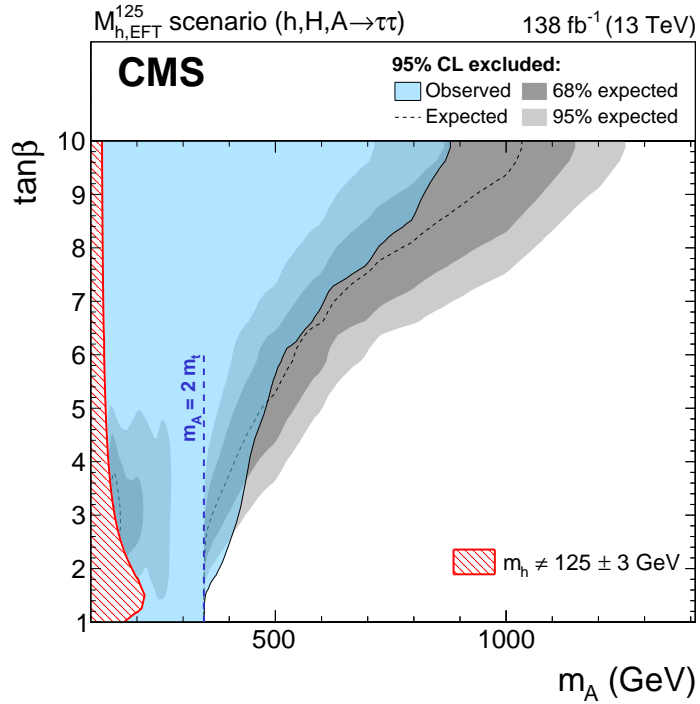
Other MSSM scenarios are tested and detailed in [40]. One scenario of note is the M_H^{125} scenario, which is the equivalent scenario to the M_h^{125} but with the observed Higgs boson being the heavier CP-even Higgs boson. Despite the local excess at a resonant mass of 100 GeV, this scenario is entirely excluded by the search. This is mostly due to the sensitivity of the b tag categories to b associated production. The local excess observed at 1.2 TeV is hard to rectify within these MSSM benchmark scenarios. The lack of any excess in the b tag categories strictly constrains the b associated production cross section times branching fraction. It is not possible within these scenarios to predict the excess of gluon fusion events within the constraints placed on b associated production.

Upper limits of 95% CL for VLQ BM 1 and 2 are shown Figure 1.29. These are drawn with respect to the leptoquark mass (m_U) and coupling (g_U). The limit on g_U decreases as m_U increases, with values of g_U ranging from 1.3 to 5.2 in VLQ BM 1 and 0.8 to 3.2 in VLQ BM 2. VLQ BM 2 has stronger exclusion limits than VLQ BM 1 due to additional right-handed couplings of the leptoquark with a b quark and a τ lepton. The observed limits fall within the central 95% intervals of the expected limits when no signal is present. The expected limits are also within the 95% confidence interval of the best fit results reported by Ref.[41] and described in Section ???. This indicates that the search is capable of detecting a part of the parameter space that can explain the anomalies observed in b physics and since no significant excess was observed in this search, new constraints are placed on the vector leptoquark phase space.

Similarly to the MSSM scenarios, the local excess at 1.2 TeV is not consistent with a VLQ BM 1 or 2 vector leptoquark. Again this is due to lack of signal in the b tag categories, where the reduction in backgrounds makes the t-channel signal with initial state radiation the dominant search option.

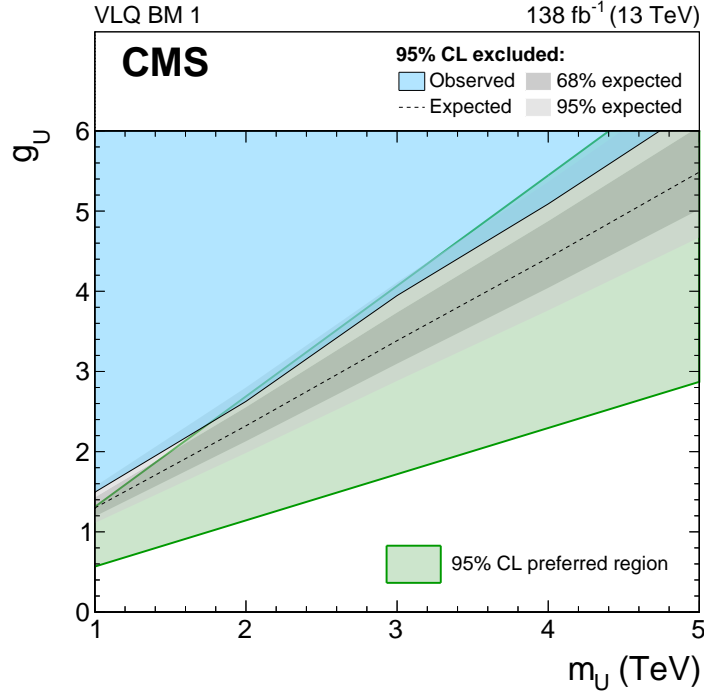


(a)

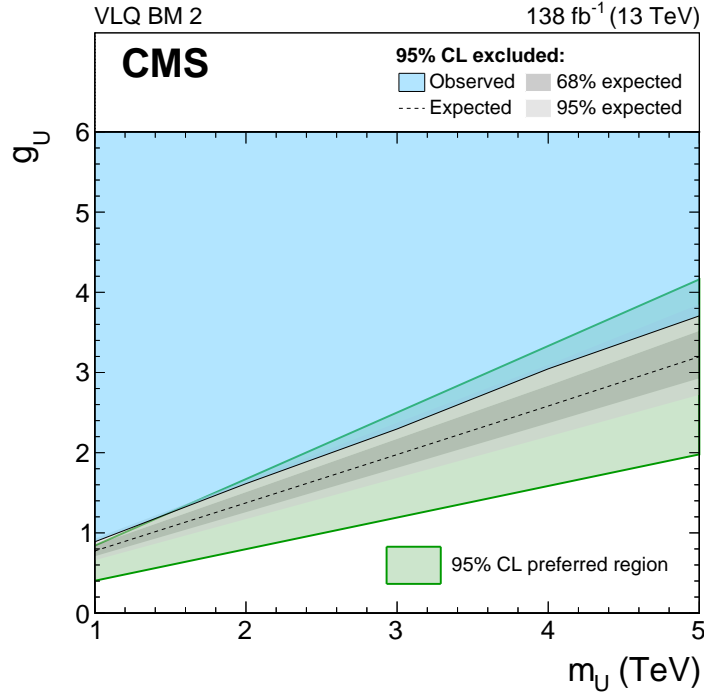


(b)

Figure 1.28: Expected and observed 95% CL exclusion contours in the MSSM M_h^{125} (a) and $M_{h,EFT}^{125}$ (b) scenarios. The exclusion limit only on background expectation is shown as a dashed black line, the dark and bright grey bands show the 68% and 95% intervals of the expected exclusion and the observed exclusion contour is shown by the blue area. The parameter space where m_h deviates by more than ± 3 GeV from the observed SM Higgs boson mass is shown by a red hatched area.



(a)



(b)

Figure 1.29: Expected and observed 95% CL upper limits on g_U in the VLQ BM 1 (a) and 2 (b) scenarios, in a mass range of $1 < m_U < 5$ TeV. The exclusion limit only on background expectation is shown as a dashed black line, the dark and bright grey bands show the 68% and 95% intervals of the expected exclusion and the observed exclusion contour is shown by the blue area. The 95% confidence interval for the preferred region from the global fit presented in Ref. [41] is also shown by the green shaded area.

Bibliography

- [1] E. Bagnaschi, H. Bahl, E. Fuchs, T. Hahn, S. Heinemeyer, S. Liebler, S. Patel, P. Slavich, T. Stefaniak, C. E. M. Wagner, and G. Weiglein, “MSSM Higgs boson searches at the LHC: Benchmark scenarios for Run 2 and beyond,” *Eur. Phys. J. C*, vol. 79, p. 617, 2019.
- [2] H. Bahl, P. Bechtle, S. Heinemeyer, S. Liebler, T. Stefaniak, and G. Weiglein, “HL-LHC and ILC sensitivities in the hunt for heavy Higgs bosons,” *Eur. Phys. J. C*, vol. 80, p. 916, 2020.
- [3] H. Bahl, S. Liebler, and T. Stefaniak, “MSSM Higgs benchmark scenarios for Run 2 and beyond: the low $\tan\beta$ region,” *Eur. Phys. J. C*, vol. 79, p. 279, 2019.
- [4] E. A. Bagnaschi, S. Heinemeyer, S. Liebler, P. Slavich, and M. Spira, “Benchmark scenarios for MSSM Higgs boson searches at the LHC,” Tech. Rep. LHCHWG-2021-001, CERN, 2021.
- [5] CMS Collaboration, “Search for additional neutral MSSM Higgs bosons in the $\tau\tau$ final state in proton-proton collisions at $\sqrt{s} = 13$ TeV,” *JHEP*, vol. 09, p. 007, 2018.
- [6] V. Khachatryan *et al.*, “Search for neutral MSSM Higgs bosons decaying into a pair of bottom quarks,” *JHEP*, vol. 11, p. 071, 2015.
- [7] P. Nason, “A new method for combining NLO QCD with shower Monte Carlo algorithms,” *JHEP*, vol. 11, p. 040, 2004.
- [8] S. Frixione, P. Nason, and C. Oleari, “Matching NLO QCD computations with parton shower simulations: the POWHEG method,” *JHEP*, vol. 11, p. 070, 2007.

- [9] S. Alioli, P. Nason, C. Oleari, and E. Re, “A general framework for implementing NLO calculations in shower Monte Carlo programs: the POWHEG BOX,” *JHEP*, vol. 06, p. 043, 2010.
- [10] T. Ježo and P. Nason, “On the treatment of resonances in next-to-leading order calculations matched to a parton shower,” *JHEP*, vol. 12, p. 065, 2015.
- [11] R. D. Ball *et al.*, “Parton distributions for the LHC Run II,” *JHEP*, vol. 04, p. 040, 2015.
- [12] R. D. Ball *et al.*, “Parton distributions from high-precision collider data,” *Eur. Phys. J. C*, vol. 77, p. 663, 2017.
- [13] A. M. Sirunyan *et al.*, “Extraction and validation of a new set of CMS PYTHIA8 tunes from underlying-event measurements,” *Eur. Phys. J. C*, vol. 80, p. 4, 2020.
- [14] T. Sjöstrand, S. Ask, J. R. Christiansen, R. Corke, N. Desai, P. Ilten, S. Mrenna, S. Prestel, C. O. Rasmussen, and P. Z. Skands, “An introduction to PYTHIA 8.2,” *Comput. Phys. Commun.*, vol. 191, p. 159, 2015.
- [15] S. Agostinelli *et al.*, “GEANT4—a simulation toolkit,” *Nucl. Instrum. Meth. A*, vol. 506, p. 250, 2003.
- [16] CMS Collaboration, “The search for a third-generation leptoquark coupling to a τ lepton and a b quark through single, pair and nonresonant production at $\sqrt{s} = 13$ TeV,” 2022.
- [17] J. Alwall, M. Herquet, F. Maltoni, O. Mattelaer, and T. Stelzer, “MadGraph 5: Going beyond,” *JHEP*, vol. 06, p. 128, 2011.
- [18] R. Frederix and S. Frixione, “Merging meets matching in MC@NLO,” *JHEP*, vol. 12, p. 061, 2012.
- [19] L. Bianchini, J. Conway, E. K. Friis, and C. Veelken, “Reconstruction of the Higgs mass in $H \rightarrow \tau\tau$ events by dynamical likelihood techniques,” *J. Phys. Conf. Ser.*, vol. 513, p. 022035, 2014.
- [20] CMS Collaboration, “Measurements of Higgs boson production in the decay channel with a pair of τ leptons in proton-proton collisions at $\sqrt{s} = 13$ TeV.” Submitted to *Eur. Phys. J. C*, 2022.

- [21] J. Alwall, S. Höche, F. Krauss, N. Lavesson, L. Lönnblad, F. Maltoni, M. L. Mangano, M. Moretti, C. G. Papadopoulos, F. Piccinini, S. Schumann, M. Trecani, J. Winter, and M. Worek, “Comparative study of various algorithms for the merging of parton showers and matrix elements in hadronic collisions,” *Eur. Phys. J. C*, vol. 53, p. 473, 2008.
- [22] S. Alioli, S.-O. Moch, and P. Uwer, “Hadronic top-quark pair-production with one jet and parton showering,” *JHEP*, vol. 01, p. 137, 2012.
- [23] R. Frederix, E. Re, and P. Torrielli, “Single-top t -channel hadroproduction in the four-flavour scheme with POWHEG and aMC@NLO,” *JHEP*, vol. 09, p. 130, 2012.
- [24] E. Re, “Single-top Wt -channel production matched with parton showers using the POWHEG method,” *Eur. Phys. J. C*, vol. 71, p. 1547, 2011.
- [25] K. Melnikov and F. Petriello, “Electroweak gauge boson production at hadron colliders through $\mathcal{O}(\alpha_s^2)$,” *Phys. Rev. D*, vol. 74, p. 114017, 2006.
- [26] M. Czakon and A. Mitov, “Top++: A program for the calculation of the top-pair cross-section at hadron colliders,” *Comput. Phys. Commun.*, vol. 185, p. 2930, 2014.
- [27] N. Kidonakis, “Top quark production,” in *Helmholtz International Summer School on Physics of Heavy Quarks and Hadrons*, p. 139, 2014.
- [28] J. M. Campbell, R. K. Ellis, and C. Williams, “Vector boson pair production at the LHC,” *JHEP*, vol. 07, p. 018, 2011.
- [29] T. Gehrmann, M. Grazzini, S. Kallweit, P. Maierhöfer, A. von Manteuffel, S. Pozzorini, D. Rathlev, and L. Tancredi, “ W^+W^- production at hadron colliders in next to next to leading order QCD,” *Phys. Rev. Lett.*, vol. 113, p. 212001, 2014.
- [30] R. J. Barlow and C. Beeston, “Fitting using finite Monte Carlo samples,” *Comput. Phys. Commun.*, vol. 77, p. 219, 1993.
- [31] J. S. Conway, “Incorporating nuisance parameters in likelihoods for multisource spectra,” in *PHYSTAT 2011*, p. 115, 2011.

- [32] A. M. Sirunyan *et al.*, “Performance of missing transverse momentum reconstruction in proton-proton collisions at $\sqrt{s} = 13$ TeV using the CMS detector,” *JINST*, vol. 14, p. P07004, 2019.
- [33] T. Junk, “Confidence level computation for combining searches with small statistics,” *Nucl. Instrum. Meth. A*, vol. 434, p. 435, 1999.
- [34] A. L. Read, “Presentation of search results: The CL_s technique,” *J. Phys. G*, vol. 28, p. 2693, 2002.
- [35] G. Cowan, K. Cranmer, E. Gross, and O. Vitells, “Asymptotic formulae for likelihood-based tests of new physics,” *Eur. Phys. J. C*, vol. 71, p. 1554, 2011. [Erratum: [doi:10.1140/epjc/s10052-013-2501-z](https://doi.org/10.1140/epjc/s10052-013-2501-z)].
- [36] G. Aad *et al.*, “Search for heavy Higgs bosons decaying into two tau leptons with the ATLAS detector using pp collisions at $\sqrt{s} = 13$ TeV,” *Phys. Rev. Lett.*, vol. 125, p. 051801, 2020.
- [37] LHC Higgs Cross Section Working Group, “Handbook of LHC Higgs cross sections: 3. Higgs properties,” Tech. Rep. CERN-2013-004, 2013.
- [38] LHC Higgs Cross Section Working Group, “Handbook of LHC Higgs cross sections: 4. deciphering the nature of the Higgs sector,” Tech. Rep. CERN-2017-002-M, 2016.
- [39] A. Denner, S. Heinemeyer, I. Puljak, D. Rebuszi, and M. Spira, “Standard model Higgs-boson branching ratios with uncertainties,” *Eur. Phys. J. C*, vol. 71, p. 1753, 2011.
- [40] CMS Collaboration, “Searches for additional Higgs bosons and vector leptoquarks in $\tau\tau$ final states in proton-proton collisions at $\sqrt{s} = 13$ TeV,” 2022.
- [41] C. Cornella, D. A. Faroughy, J. Fuentes-Martin, G. Isidori, and M. Neubert, “Reading the footprints of the B-meson flavor anomalies,” *JHEP*, vol. 08, p. 050, 2021.